ELSEVIER

Journal of Structural Geology 29 (2007) 961–982

JOURNAL OF STRUCTURAL GEOLOGY

www.elsevier.com/locate/jsg

A kinematic model for the Rinconada fault system in central California based on structural analysis of *en echelon* folds and paleomagnetism

Sarah J. Titus [a,*], Bernard Housen [b], Basil Tikoff [c]

[a] *Department of Geology, Carleton College, One North College St., Northfield, MN 55057, USA*
[b] *Department of Geology, Western Washington University, 516 High Street, Bellingham, WA 98225, USA*
[c] *Department of Geology and Geophysics, University of Wisconsin, 1215 West Dayton Street, Madison, WI 53706, USA*

Received 9 August 2006; received in revised form 2 February 2007; accepted 6 February 2007
Available online 20 February 2007

Abstract

Deformation associated with the Rinconada fault, one of the major strands of the San Andreas fault system in central California, is accommodated by both discrete fault offset (~18 km) and distributed off-fault deformation. *En echelon* folds adjacent to the Rinconada fault were studied in detail at two locations, near Williams Hill and Lake San Antonio, to characterize the magnitude and style of distributed deformation. The obliquity between fold hinges and the local strike of the fault was 27° and 14° at these two sites, respectively. Systematic outcrop-scale fault displacement measurements along roadcuts indicate that the maximum horizontal elongation occurs parallel to local fold hinges and ranges from 4 to 9%.

We used the orientation and stretch of fold hinges to construct a transpressional kinematic model for distributed deformation. This modeling suggests a 20–50° angle of oblique convergence, 5 km of fault-parallel wrench deformation, and 2–4 km of fault-perpendicular shortening. Between 3° and 16° of clockwise rotation is also predicted by our model. This rotation is independently confirmed by a $14 \pm 7°$ vertical axis rotation from regional paleomagnetic analyses. Integrating the regional discrete and distributed components of deformation suggests that the Rinconada fault system is 80% strike-slip partitioned.

Keywords: *En echelon* folds; Paleomagnetism; Rinconada fault; Strain partitioning; Transpression

1. Introduction

Transpression is a three-dimensional model for deformation that includes both transcurrent and convergent components of motion across a deforming system (e.g. Harland, 1971; Sanderson and Marchini, 1984; Fossen and Tikoff, 1993; Lin et al., 1998; Jones et al., 2004). Because the relative motion between the Pacific and North American plates is obliquely convergent (e.g. Atwater and Stock, 1998), transpression can be used to understand the kinematics of deformation for the San Andreas fault system. The angle of oblique convergence, α, for the entire system is approximately 5° in central California (Argus and Gordon, 2001) indicating that deformation predominantly involves wrench motion with only a small component of contraction across the system.

In detail, different geologic structures may accommodate the wrench and contraction components of deformation (e.g. Molnar, 1992; Dewey et al., 1998) through strike-slip partitioning (e.g. Tikoff and Teyssier, 1994; Jones and Tanner, 1995; Teyssier et al., 1995; Teyssier and Tikoff, 1998). Previous estimates have suggested 95–100% strike-slip partitioning for the San Andreas fault system based on borehole breakouts (Zoback et al., 1985) and fold hinge orientations (Mount and Suppe, 1987; Zoback et al., 1987; Tikoff and Teyssier, 1994; Teyssier et al., 1995; Miller, 1998; Teyssier and Tikoff, 1998). This high degree of strike-slip partitioning implies that discrete fault offsets accommodate almost exclusively wrench motion and distributed deformation between the fault strands accommodates contraction with little or no wrench motion.

* Corresponding author.
E-mail address: stitus@carleton.edu (S.J. Titus).

0191-8141/$ - see front matter © 2007 Elsevier Ltd. All rights reserved.
doi:10.1016/j.jsg.2007.02.004

This study is focused on characterizing deformation across the Rinconada fault system in central California to investigate how and where the wrench and contraction components of bulk plate motion are accommodated for this portion of the San Andreas fault system. We combine the map-patterns of *en echelon* folds adjacent to the fault with analysis of small-displacement faults in the region to construct a kinematic model of deformation. Vertical axis rotations, derived from paleomagnetic analyses provide an independent check on our kinematic model. Both data sets support the conclusion that the Rinconada fault system is 80% strike-slip partitioned. This lower degree of strike-slip partitioning has implications for how deformation is partitioned across the San Andreas fault system.

2. Geologic setting

2.1. Rinconada fault system

Our study focuses on the Rinconada fault system, a 250 km-long strand of the San Andreas fault system in central California (Fig. 1). Deformation across this portion of the fault system is accommodated both by discrete dextral fault offset as well as distributed off-fault deformation.

Discrete offsets of a variety of units suggest that the Rinconada fault has been an active dextral strike-slip fault since the early Tertiary, with a possible proto-Rinconada fault in the Late Cretaceous (Nilsen and Clarke, 1975). The Pliocene Pancho Rico Formation, a marine sandstone (Durham and Addicott, 1965), and the Paso Robles Formation, a gravel-rich alluvial deposit found throughout the Salinas Valley (Galehouse, 1967), have both been displaced 18 km laterally by the Rinconada fault (Durham, 1965a). There is no evidence of Holocene offset along the fault (Dibblee, 1976).

The distributed deformation component is characterized at the surface by numerous *en echelon* folds mapped in sedimentary rocks within ~10 km on either side of the fault (e.g. Taliaferro, 1943a,b; Durham, 1964, 1965b, 1968; Compton, 1966; Dibblee, 1976). Folds are generally symmetric and upright with moderate limb dips. Fold hinges do not cross the Rinconada fault and are generally oblique in an anticlockwise direction to the local strike (300–320°) of the fault. Many of

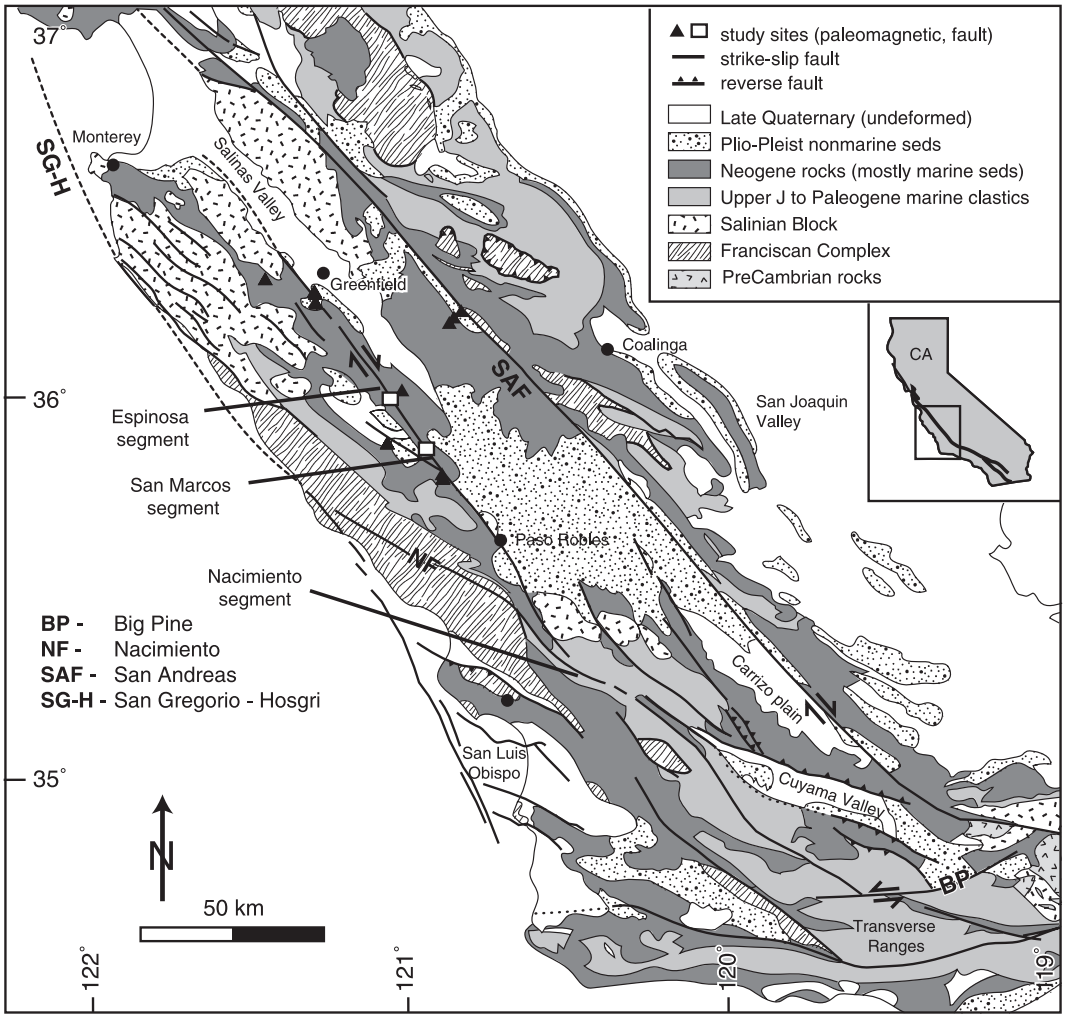

Fig. 1. Map of central California showing major geographic features and place names. Boxes show location of detailed fault population measurements. Triangles show the locations of paleomagnetic sites. Modified from Jennings et al. (1977) and Page et al. (1998).

the *en echelon* folds closest to the Rinconada fault are within the Miocene Monterey Formation, an assemblage of marine sedimentary rocks including limestones, dolostones, mudstones, shales and silica-rich horizons found along much of coastal California (e.g. Isaacs, 1980). Sub-parallel folds have also developed in the younger Pancho Rico Formation and Paso Robles Formations as well as in older Cretaceous and early Tertiary sedimentary rocks (Dibblee, 1976).

We focus primarily on the Monterey Formation, ideal for this study because: (1) it is exposed across much of central California but the magnitude of deformation, as expressed by *en echelon* folding, varies locally (e.g. Dibblee, 1976; Jennings et al., 1977; Snyder, 1987); (2) the stable natural remanence recorded by rocks of the Monterey Formation (e.g. Hornafius, 1985; Omarzai, 1996) permits paleomagnetic analyses of sites across the region; and (3) the history of deposition and deformation is intimately linked to the development of the plate boundary system (described in Section 2.2; Blake et al., 1978; Graham, 1978) ensuring that deformation recorded by these sedimentary rocks is contemporaneous with deformation on the San Andreas fault system.

2.2. Tectonic context

The Monterey Formation was deposited during the middle to late Miocene in deep basins along the California margin (Blake et al., 1978; Pisciotto, 1978; Pisciotto and Garrison, 1981; Ingle, 1981). Deposition occurred during a period of oblique divergence between the Pacific and North American plates following passage of the Mendocino Triple Junction (Blake et al., 1978). The relative plate motion changed from oblique divergence to oblique convergence after deposition of the Monterey Formation, resulting in a shift to terrestrial sedimentation. We review estimates for the timing of this shift from transtension to transpression from different data sets to bracket the initiation of distributed deformation adjacent to the Rinconada fault.

Plate reconstruction studies suggest a wide range of timing estimates. Using global plate motion circuits, Atwater and Stock (1998) propose the earliest estimates of transpression at ~8 Ma. Previous studies found the shift between ~3.5 and 5 Ma based on hotspot tracks such as the Hawaiian-Emperor chain (Cox and Engebretson, 1985; Pollitz, 1986; Harbert, 1991).

Studies of uplift throughout the Coast Ranges provide an intermediate estimate for the timing of transpression. Ducea et al. (2003) demonstrate that uplift in the Santa Lucia range began at ~6 Ma based on helium ages from apatite. Miller (1998) suggests that the southern Diablo Range and Temblor Range began their current phase of uplift by at least 5.4 Ma. Using the topography across multiple transects of the San Andreas fault system as an indication of uplift magnitude, Argus and Gordon (2001) found that present topography required 6 m.y. to form based on current rates of shortening.

Geologic analysis of folding and faulting indicates several periods of contraction in the region starting between 11 and 7 Ma with the major onset of deformation at ~3.5 Ma (Page, 1981; Page et al., 1998). Folds in the Pliocene Paso Robles Formation in the northern Santa Lucia Range near the Rinconada fault are nearly parallel to those in underlying folded formations, implying that the major episode of folding and faulting took place in the Pliocene or later (Compton, 1966). Given the constraints from plate motion and uplift studies, we cannot rule out earlier episodes of deformation of the Monterey Formation that may have caused similar orientations of geologic structures in units with different ages (e.g. Tavarnelli and Holdsworth, 1999). Thus, we bracket the timing of fold initiation in the region between 6 and 8 Ma (earliest) to 3.5 Ma (latest).

3. Fold analysis

3.1. Theory

Before describing our kinematic reconstructions using naturally deformed folds, it is first useful to review models of folding during progressive deformation. Under controlled boundary conditions, physical and numerical models predict that fold hinges initiate parallel to the maximum horizontal infinitesimal stretching direction (perpendicular to the maximum compressive stress; Graham, 1978; Odonne and Vialon, 1983; Tikoff and Peterson, 1998) regardless of the viscosity of the folded layers (James and Watkinson, 1994). The angle of fold initiation is controlled by the angle of oblique convergence (Fig. 2). Folds that form in pure contraction ($\alpha = 90°$; Fig. 2a) are parallel to the deforming zone boundaries whereas folds that form in pure wrench deformation ($\alpha = 0°$; Fig. 2c) initiate at 45° to the boundaries. The angle between fold hinges and the zone boundaries falls between these two end-members in cases of transpression ($0° < \alpha < 90°$; Fig. 2b).

Once initiated, all folds except those formed in pure contraction rotate towards the shear plane and their hinges necessarily elongate during progressive deformation (Fig. 3a). Physical models confirm this prediction, where fold hinge elongation is accommodated by a variety of structures such as strike-slip and normal faults (Wilcox et al., 1973), ductile boudinage (Richard et al., 1991) or thinning (Tikoff and Peterson, 1998) during continued deformation. The magnitude of fold hinge rotation and elongation is inversely dependent on α: smaller α angles lead to greater rotation and elongation of the fold hinges for the same total fold shortening. Quantifying this inverse relationship is complicated slightly by the interpretation of fold hinges as either (1) passive markers that follow the path of a material line (e.g. Sanderson, 1973; Ramsay, 1979; Jamison, 1991; Fossen and Tikoff, 1993), or as (2) active markers that remain parallel to the maximum horizontal finite strain axis (Wilcox et al., 1973; Treagus and Treagus, 1981; Krantz, 1995).

Fig. 3 allows for comparison between passive and active fold rotation models. In both models, deformation is broken into many small increments (Tikoff and Fossen, 1993), in order to track a fold during steady-state deformation (i.e. consistent angle of oblique convergence). In the passive fold rotation model, we track the material line that began parallel to the

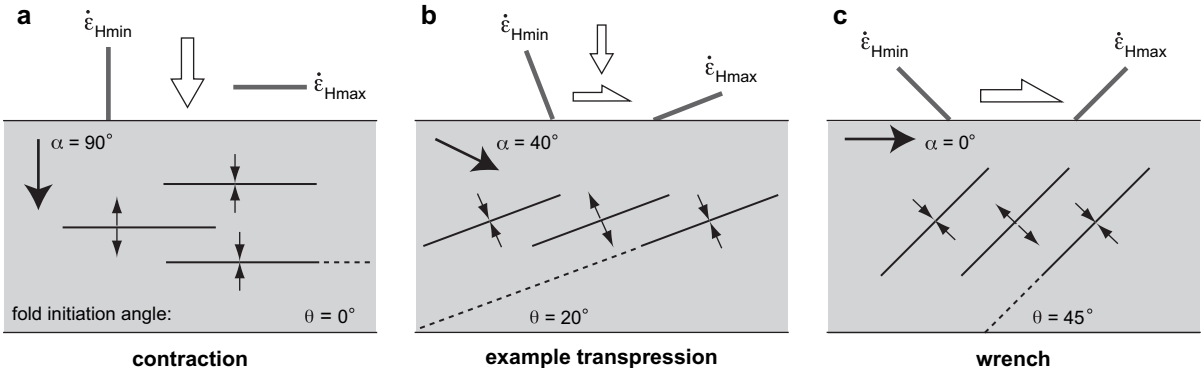

Fig. 2. Cartoon of fold formation in (a) pure wrench deformation, (b) transpression, and (c) pure contraction where each gray box represents the map view (*xy* plane) of a deforming region. Because deformation is accommodated by movement in the *z*-direction, the zone does not elongate parallel to its boundaries. White arrows denote the bulk motion, gray lines show the orientation of the maximum $\dot{\varepsilon}_{Hmax}$ and minimum $\dot{\varepsilon}_{Hmin}$ horizontal instantaneous stretching directions, black arrows denote the angle of oblique convergence, α, and θ shows the angle of fold initiation. Progressive deformation would require fold rotation in cases (a) and (b), and the angle θ would become more acute relative to the shear zone boundary through time.

maximum horizontal instantaneous stretching direction ($\dot{\varepsilon}_{Hmax}$ in Fig. 2) for each increment of deformation (Jamison, 1991). In the active fold rotation model, we find the orientation and stretch of the horizontal maximum finite strain axis, assumed to be parallel to the fold hinge, for each increment of deformation.

The primary difference between passive and active rotations in these graphs arises because material lines always rotate faster than the finite strain axis under the same boundary conditions (Lister and Williams, 1983). The difference between the two models is therefore most noticeable in the plot of hinge orientation versus shortening (Fig. 3b). For a given α and percent shortening, the orientation of folds may differ by up to 5° between the two models. In contrast, there is little difference at moderate strains in the plot of fold shortening versus hinge parallel elongation (Fig. 3c).

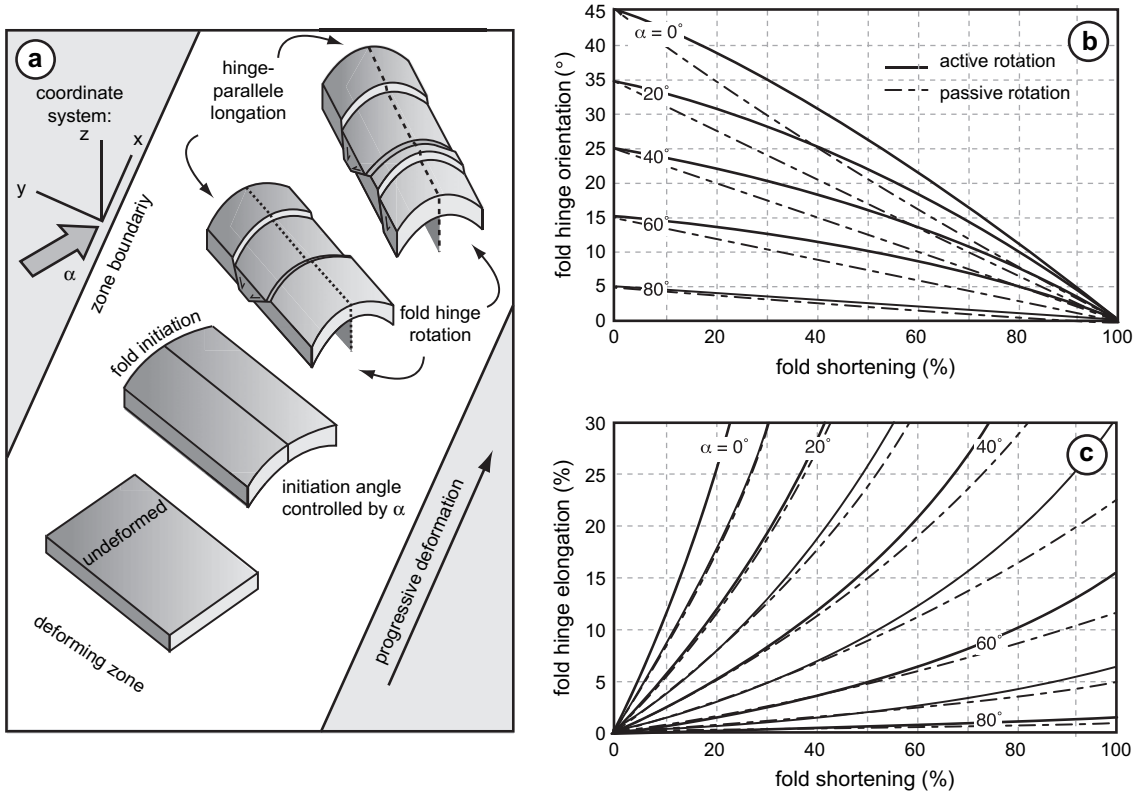

Fig. 3. (a) Cartoon illustrating fold behavior transpression, where deformation of one fold increases progressively toward the upper right-hand corner. The white zone (*xy* plane) indicates the boundaries of the actively deforming area, where the *x*-axis is parallel to the shear zone boundaries (shear direction). With progressive deformation, note (1) the decreasing angle between the fold axial plane and the shear direction, and (2) the increasing magnitude of hinge-parallel elongation (see fold hinge lines), accommodated here by normal faulting. The graphs in (b) and (c) quantify the angle of oblique convergence responsible for a particular fold hinge orientation and magnitude of hinge-parallel elongation for both active (solid line) and passive (dotted line) fold rotation.

High strains are required to distinguish between active and passive rotations, greater than those typically observed in natural examples (e.g. Little, 1992) or achieved in physical experiments (e.g. Tikoff and Peterson, 1998). Fold hinge orientation is a more sensitive recorder of deformation that, when combined with estimates of hinge-parallel elongation or fold-perpendicular shortening, can be used to predict the angle of oblique convergence responsible for folding in a region.

We prefer the active rotation fold model, which is supported by theoretical models (e.g. Treagus and Treagus, 1981) and physical experiments of folding in transpression (Tikoff and Peterson, 1998). Further, active rotation provides a minimum estimate of the total distributed deformation. Although graphical results of kinematic modeling are shown for both active and passive fold hinge rotations in this paper, numerical results are only reported for active rotation.

3.2. Application to the Rinconada fault system

To characterize fold hinge orientations in the study area, a 5×5 km fault-parallel and fault-perpendicular grid was superimposed onto maps of the Rinconada fault. For this analysis, we assumed that fold hinges were horizontal so map patterns could be used. This assumption is reasonable given the shallow plunges of most folds in the map region (Dibblee, 1976). For each fold contained within a 5×5 km box, the angle between the two-fold hinge endpoints either within or along the margins of the box was measured. These orientations were then compared to the strike of the nearest section of the Rinconada fault, allowing characterization of fold hinge orientations within $\pm$2.5 km, 2.5–7.5 km, and >7.5 km from the Rinconada fault (Table 1).

This grid-based analysis was designed to account for two characteristics of folds adjacent to the Rinconada fault (see fold map patterns in Fig. 4): (1) many folds have arcuate hinges that change orientation by up to 40–50°, and (2) fold hinge length varies by an order of magnitude ($\sim$2 to 20 km). Both characteristics may be due to coalescence of shorter folds formed at the same time and under the same applied stresses and boundary conditions (Ghosh and Ramberg, 1968). The grid size was therefore chosen to be large enough to measure the orientation of at least one fold hinge and often several fold hinges at most distances from the fault, but small enough to exclude the longest fold hinges within a single box. Consequently, the same fold hinge may be measured more than once in this gridding method. However, this is more likely to occur with longer fold hinges and can better reflect the changing orientations of fold hinges and the fault strike.

The greatest number of folds is nearly always observed within 2.5 km of the fault and the obliquity between fold hinges and the relative fault orientation is $\sim$10° to 30° (Table 1). The clear exception to this pattern is the Nacimiento 2 map (Fig. 8 from Dibblee, 1976) where there are more folds away from the fault and the obliquity is 5° or less for all distances from the fault. For this segment of the Rinconada fault, the strike is more N-trending and the fault passes through older rocks in Cuyama Valley than elsewhere along strike (Fig. 1). In this paper, we are particularly interested in the results from the Espinosa and San Marcos segments of the Rinconada fault. These sections of the fault correspond to the locations where we have detailed measurements of small-scale faults (Section 4).

3.2.1. Espinosa segment

The Espinosa segment of the Rinconada fault (Fig. 4a) has the greatest number of folds developed adjacent to the fault (Table 1). Typically, folds < 7.5 km from the fault are within the Monterey Formation whereas those >7.5 km are in the younger Pancho Rico and Paso Robles Formations. The obliquity between fold orientations and the fault does not change systematically with distance across the fault. Fold limb dips vary across the region between 10° and 50°, but more typically range from 20° to 35° (Dibblee, 1976). The average orientation of all fold hinges on this map, 27°, is used in our kinematic analysis (Section 5).

3.2.2. San Marcos segment

The San Marcos segment of the Rinconada fault (Fig. 4b) also has numerous folds (Table 1), although most folds developed southwest of the main fault trace. Within 2.5 km of the Rinconada fault, fold hinges make an acute angle with the fault (14°) and have developed in Miocene and younger rocks. At greater distances from the fault, fold hinge obliquity increases to 20–24° with folds developed in Upper Cretaceous

Table 1
For each map from Dibblee (1976), we report the average orientation of the Rinconada fault, the average number of folds from 5×5 km grid boxes at different distances from the Rinconada fault, and the relative orientation of folds with respect to the Rinconada fault.

Dibblee (1976) Map	Fault orientation	Average number of folds per grid box			Average obliquity between folds and the Rinconada fault			
		0–2.5	2.5–7.5	>7.5	0–2.5	2.5–7.5	>7.5	All
Nacimiento 1	138 ± 13	2.5	2.0	2.3	14 ± 12	20 ± 15	14 ± 16	16 ± 15
Nacimiento 2	143 ± 11	1.5	1.1	2.1	3 ± 9	2 ± 13	5 ± 20	4 ± 15
Rinconada	123 ± 12	0.8	1.1	1.0	23 ± 15	9 ± 16	21 ± 8	16 ± 16
Espinosa	125 ± 7	7.4	4.2	4.1	23 ± 13	32 ± 20	25 ± 13	27 ± 17
San Marcos	131 ± 3	5.1	2.7	2.9	14 ± 13	24 ± 11	20 ± 9	18 ± 12
Average	132 ± 13				17 ± 14	23 ± 19	17 ± 15	19 ± 17

Orientations are reported with 1σ standard deviations.

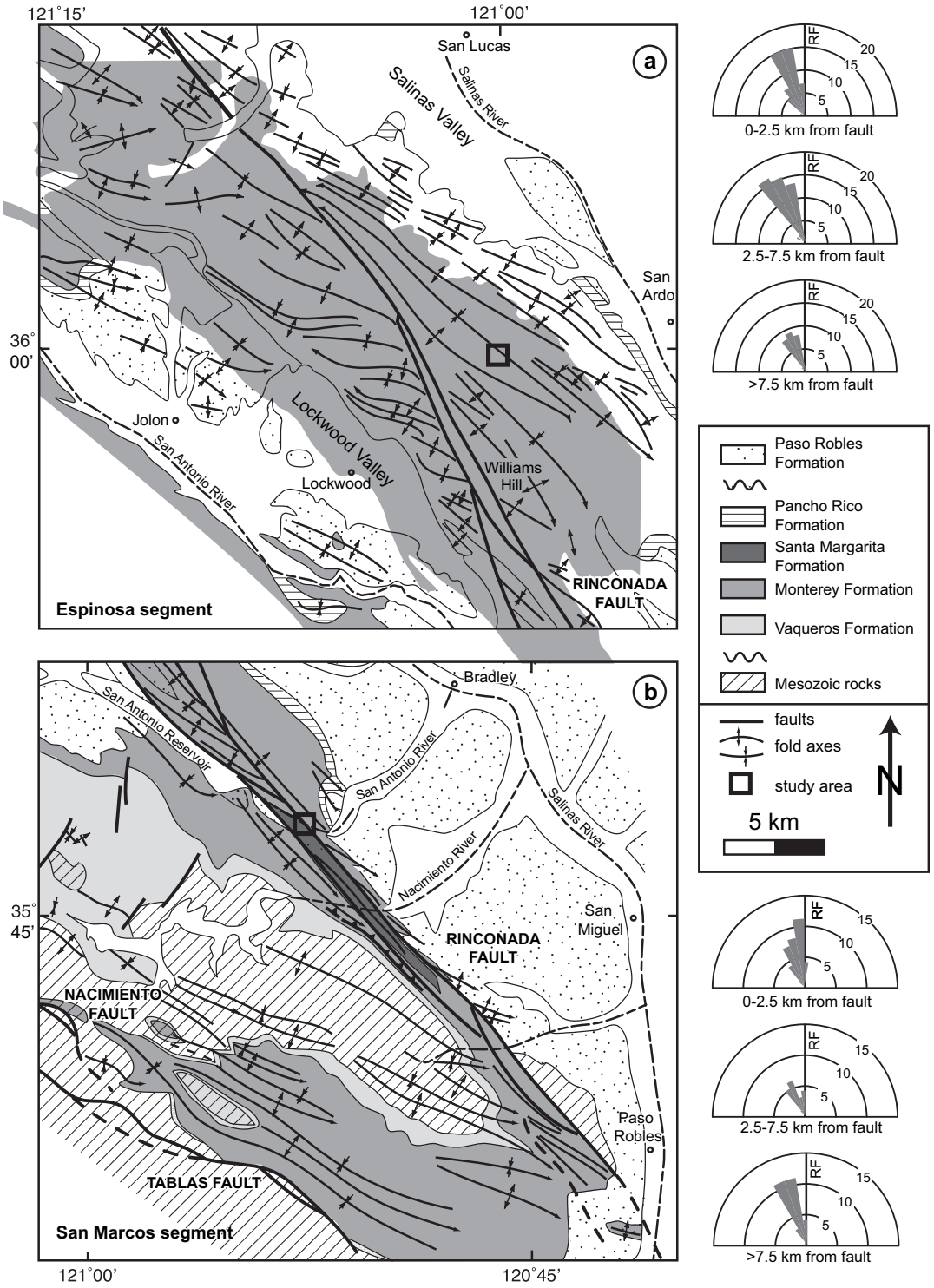

Fig. 4. Map of the (a) Espinosa and (b) San Marcos segments of the Rinconada fault. Modified from Dibblee (1976). Boxes denote location of fault population study areas at (a) Williams Hill and (b) Lake San Antonio. Rose diagrams illustrate the relative fold hinge orientations with increasing distance from the Rinconada fault (RF) from Table 1. Note that rose diagrams are related to relative orientation between the fault and fold axes and not related to geographic space.

through Tertiary rocks. Fold limb dips also vary; the average dip for near-fault folds is 60–70° but dips decrease to 25–35° for the far-fault folds (Dibblee, 1976). In our kinematic modeling (Section 5), we break this map area into two regions reflecting the different fold orientations and different fold limb dips across this map area.

4. Fault population analysis

4.1. Study locations

Faults in the Monterey Formation occur at many scales of observation (Fig. 5). Populations of outcrop-scale faults were

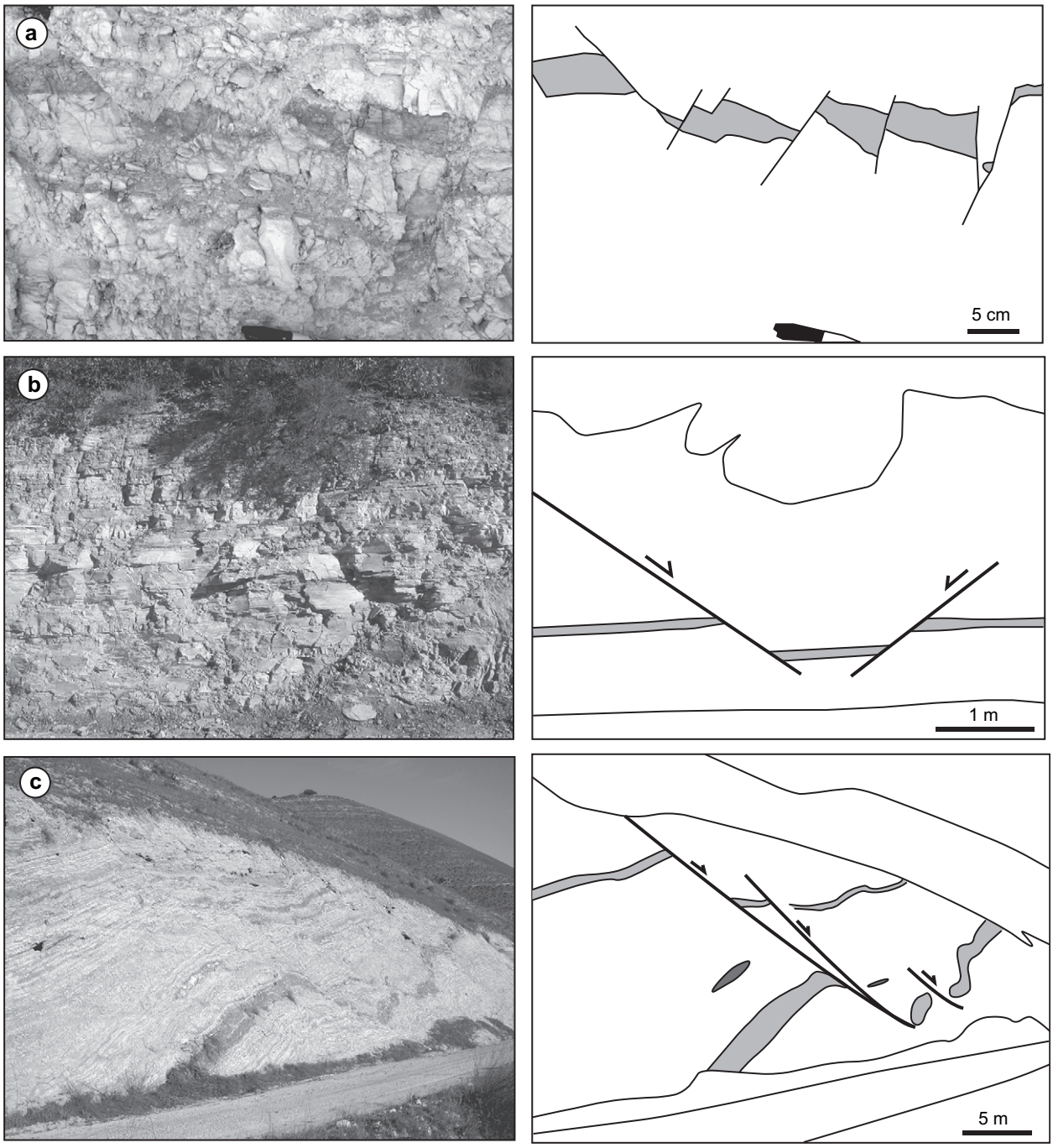

Fig. 5. Photographs showing typical faults at a variety of scales in the Monterey Formation at the two study sites. The photograph (a) shows the small faults location and (b) shows a conjugate normal fault pair, both from Williams Hill. Photograph (c) is an oblique view of faults along traverse 4 from Lake San Antonio, where more distinctive lithologic differences between sedimentary layers are observed.

measured at two sites (Williams Hill and Lake San Antonio) to quantify the magnitude and orientation of elongation in the region. The lithology of the upper Monterey Formation at both study locations is dominantly mudstones and siltstones. Because of the relative homogeneity within the Monterey Formation and well-developed joint sets, it was not always straightforward to measure separations along faults. Fault separations were more clearly observed when specific layers had color or lithologic distinctions, such as coarser-grained texture or organic-rich horizons (Fig. 5). Roadcuts provided the best continuous vertical and horizontal exposures for detailed fault population analysis. We measured faults along available roadcuts with consistent orientations for distances between 100 and 300 m. Fault locations and orientations from both study sites are shown in Fig. 6 and discussed in more detail below.

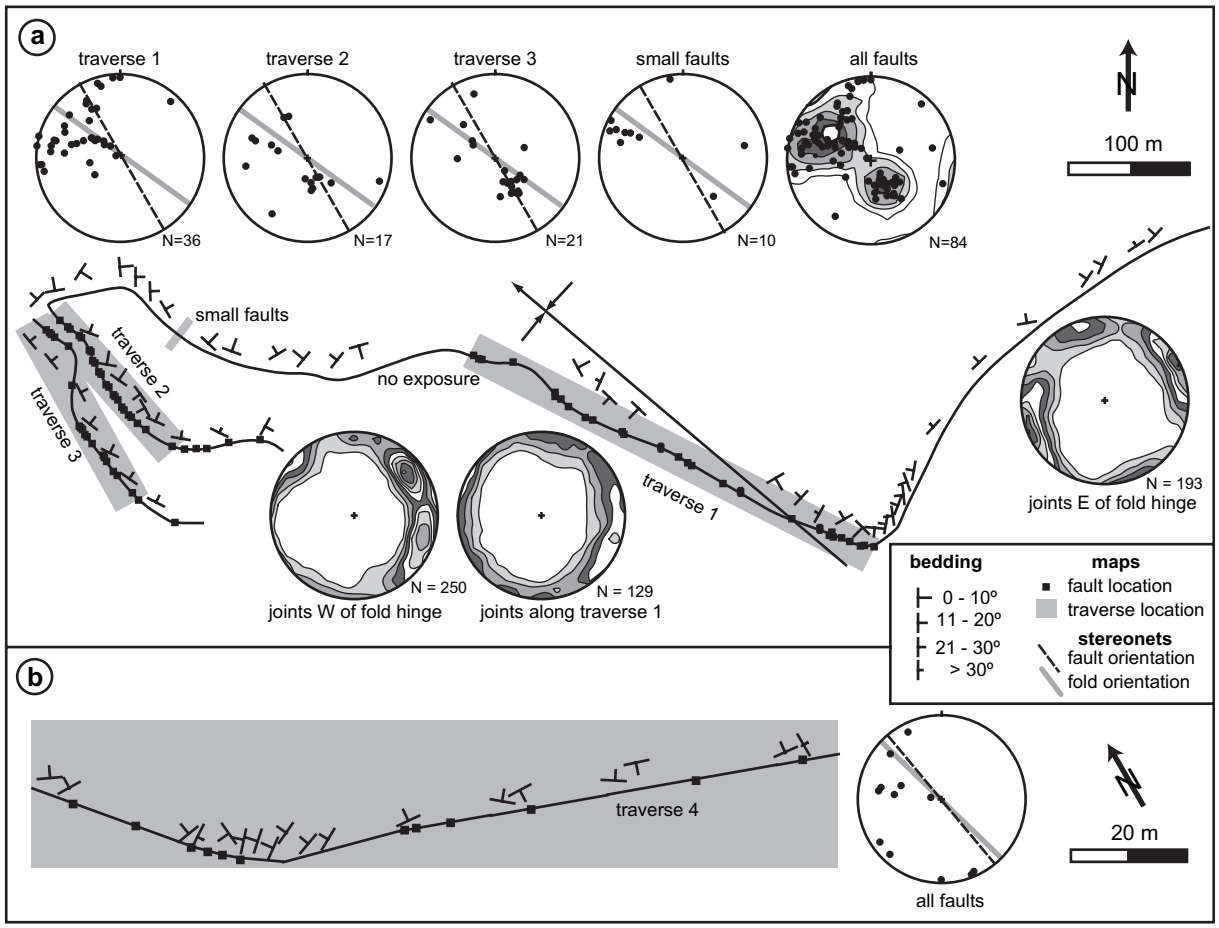

Fig. 6. Maps of the fault traverses for (a) Williams Hill and (b) Lake San Antonio. Traverse locations and lengths are denoted by gray areas. Black boxes indicate the location of faults measured at each site. Equal area, lower-hemisphere projections show poles to fault planes for each traverse with the orientation of the local fold hinge and the Rinconada fault. Stereographic projections for Williams Hill also show joint measurements for each limb of the local fold.

4.1.1. Williams Hill

The Williams Hill site, located between Lockwood and Salinas Valleys (Fig. 1), is ~3 km from the Espinosa segment of the Rinconada fault. The road passes through an upright syncline trending 310°, which plunges shallowly to the north and has gentle to moderate limb dips between 10° and 30° (Fig. 4a; Dibblee, 1976). Detailed joint measurements from numerous locations along roadcuts at Williams Hill show three dominant fracture sets where two sets are perpendicular to bedding and one is parallel to bedding (Fig. 6). These fracture patterns are common in the Monterey Formation and are often attributed to synfolding deformation (e.g. Snyder, 1987; Dholakia et al., 1998).

We measured faults along three traverses at Williams Hill (denoted as 1, 2, and 3 in Fig. 6; Appendix A). Two sets of faults are observed for the fault population at this site, both striking NE–SW, and dipping moderately either to the NW or the SE (Fig. 6). We also report data from a 1.6-m transect labeled "small faults" in Fig. 6, where several faults offset a particularly distinctive marker bed (Fig. 5a; Appendix A). Given the limited length of this traverse, the small faults data set may not be representative of bulk regional deformation.

4.1.2. Lake San Antonio

The site near Lake San Antonio is between two major 310°-trending fault splays of the San Marcos segment of the Rinconada fault, less than 1 km from either splay (Fig. 6b; Dibblee, 1976). Faults were measured along a single traverse (denoted as 4 in Fig. 6) on the southwest limb of a nearly fault-parallel anticline (Fig. 4b; Appendix A). Fault strikes were generally NE–SW but unlike the Williams Hill site, only SE-dipping faults are observed. Fault separations were much easier to quantify here because of the presence of distinctive marker beds (Fig. 5c), although fewer total faults were present along the traverse than those from Williams Hill.

4.2. Estimating one-dimensional elongation

In the field, fault separations were measured in the dip direction of each fault and wherever possible, the separation was measured precisely. In some cases, it was necessary to estimate the separation when offset units were along the tops of roadcuts (at levels too high to measure precisely). Most faults show an apparent normal separation, although it was not possible to rule out a component of strike-slip motion due to a lack of slickenline preservation on the fault surfaces.

For this analysis, we assumed that movements were strictly down-dip. The consequences of this assumption are discussed in more detail below.

Measured fault heaves were projected onto the average roadcut orientation to find the cumulative change in length (ΔL) for each traverse. Since the final traverse length L_f is known, we can compute the original traverse length ($L_f - \Delta L$) to estimate the simple one-dimensional elongation for each traverse. Note that each traverse is bounded by faults in order to avoid biasing the total length (and therefore elongation) by unconstrained distances on either end of the traverse. Horizontal heaves from the two bounding faults were not included in the analysis.

The one-dimensional elongation estimates from each traverse are summarized in Table 2. The magnitude of elongation varies from 1.0 to 6.4% for the four traverses. In addition to variation in finite strain, the observed range of elongation values may be due to local characteristics of each site including lithologic variation, quality of exposure, and traverse orientation. For example, traverses 1 and 4 had the greatest vertical relief along the roadcuts (>10 m), increasing the likelihood that large displacements could be observed, whereas traverses 2 and 3 were along shorter roadcuts (~3 m tall).

At Williams Hill, where more data have been collected, the maximum elongation for the three traverses is 3.9%. Elongation at the small faults site (6.1%) is the largest value obtained from Williams Hill but, as mentioned previously, may not be representative of the bulk deformation in the region. The elongation estimate is 6.4% for Lake San Antonio. Note that these values are really ''apparent elongations'' since faults may have a component of strike-slip motion that we cannot quantify in the field.

4.3. Revised elongation estimates

Elongation calculated from normal fault populations typically underestimates the total elongation due to incomplete sampling of small faults with unobservable offsets (e.g. King and Cisternas, 1991; Marrett and Allmendinger, 1991; Walsh et al., 1991). In order to quantitatively estimate the contribution from these small-displacement faults, we applied theoretical fault displacement population analysis assuming a fractal size distribution of fault heaves (e.g. Scholz and Cowie, 1990; Walsh et al., 1991).

Gross and Engelder (1995) applied this method successfully to revise elongation estimates from traverses within the Monterey Formation in the Transverse Ranges. We used their study as a model for our own fault population analysis. In brief, fault population data are plotted as the log of each fault displacement h_i versus the log of the corresponding fault number ($1 \leq i \leq n$, where 1 is the largest displacement fault and n the smallest). An example is shown in Fig. 7a. Faults with intermediate displacements have a linear relationship, and the slope of this line, $-C$, can be used to estimate the missing elongation due to unsampled small-displacement faults. See Marrett and Allmendinger (1992) and Gross and Engelder (1995) for more detailed summaries of both the methodology and its application to data sets at several scales.

Our revised elongation estimates are reported in Table 2. For traverses 1–3, revisions increase the elongation estimates by 0.2–3.1%. The range in values reported for traverses 1 and 2 is due to a variety of slopes, $-C$, that can potentially fit the linear portion of the data. Due to small sample sizes at traverse 4 (from Lake San Antonio) and the small faults sites, we were not able to revise the original elongation estimates.

This fractal distribution model was also applied to the entire fault population at Williams Hill illustrated in Fig. 7a. For this estimate, we projected fault heaves onto the local fold hinge orientation (310°) to compare fault heave magnitudes along a single azimuth. Subsets of the intermediate-displacement faults in this model can be fit by a variety of different slopes, $-C$, suggesting that our measured fault population elongation represents 40–90% of the true elongation. The line shown in Fig. 7a shows the best-fit slope to the greatest number of faults and indicates that our population sampled ~80% of the true elongation.

To summarize, the original fault population data from Williams Hill suggested 1–4% elongation for the three traverses. Revisions for each traverse, based on fractal size distribution of fault displacements, suggested one-dimensional elongation as high as 6.5%, and analysis of the entire fault population suggested that our sampling captured approximately 80% of the total elongation at this site. Thus, $5 \pm 1\%$ is a reasonable average estimate of elongation for this area. This detailed analysis was not possible at Lake San Antonio because fewer faults were measured. The 6.4% elongation from traverse 4 is probably a minimum estimate. In the absence of more data, we use the revision ranges (up to 3%) from Williams Hill as a guide for the fault population at Lake San Antonio, indicating that the upper bound for elongation may be as high as ~9%.

Table 2
Summary of data from different fault traverses

Traverse	L_f (cm)	Average orientation (°)	Fold axis orientation (°)	# Faults	ΔL dip dir (cm)	ΔL traverse (cm)	Elongation (%)	Revised elongation (%)
1	31 027	115	130	35	1120	1018	3.4	3.6–6.5
2	10 795	140	130	15	439	417	3.9	4.3–4.9
3	17 245	155	130	16	205	167	1.0	1.6
4	12 600	120	134	13	830	754	6.4	–
Small faults	160	110	130	8	9.4	9.2	6.1	–

L_f is the total length of the traverse. ΔL is the sum of all fault heaves reported first in the dip direction of each fault and second projected onto to the average orientation of the outcrop. The method for computing one-dimensional extension is described in Section 4.2 and for computing revised extension in Section 4.3.

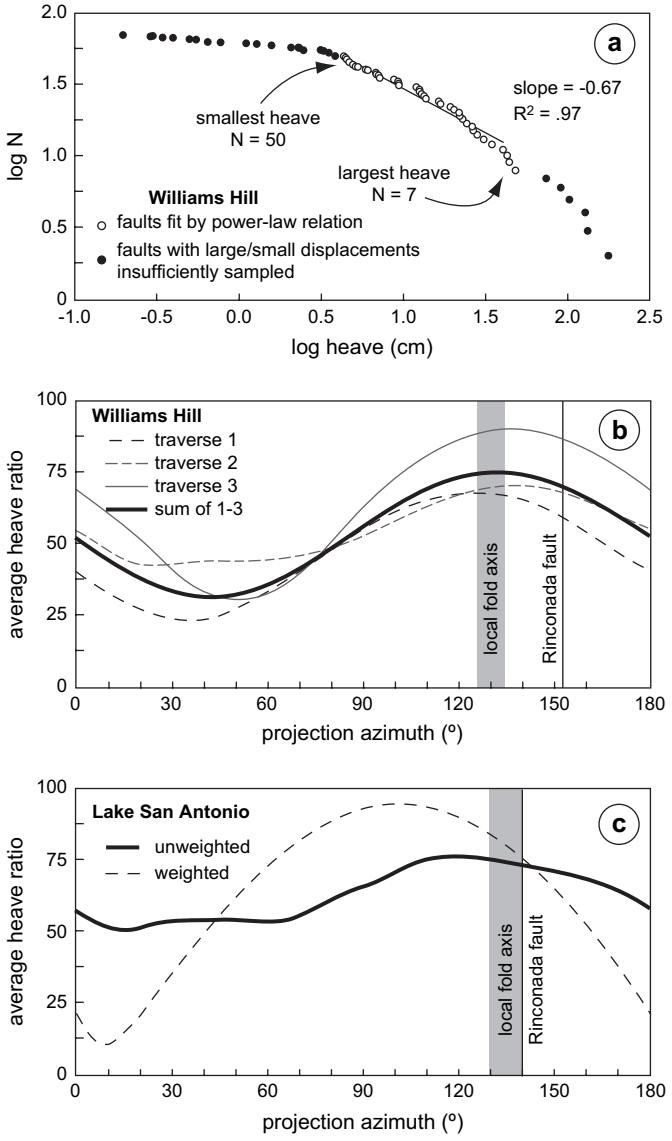

Fig. 7. Fault population information from the fault traverses. (a) Theoretical fault population displacement analysis for all faults at Williams Hill. Similar graphs were made for each traverse resulting in the revised estimates in Table 2. Fault projection plots for (b) Williams Hill and (c) Lake San Antonio, showing the average value of apparent fault heave in a particular orientation versus total heave in the dip direction of the fault. Maximum horizontal displacements are observed parallel to the fold hinge orientation for all three traverses at Williams Hill, as well as the entire fault population. At Lake San Antonio, fewer faults result in a less well-defined pattern of horizontal displacements, but a maximum is observed near local fold orientations. The dotted line shows the results if fault displacements are weighted by displacement magnitude. See text for details.

4.4. Orientation of elongation

The local fold orientation at Williams Hill is 130° while the three traverses had azimuths of 115°, 140°, and 150°. At Lake San Antonio, the fault traverse and local fold hinge are parallel (120°). Thus the elongation estimate from Lake San Antonio represents hinge-parallel elongation while the Williams Hill data are not precisely hinge-parallel elongations.

We developed a graphical method to illustrate the effect of traverse orientation (at a variety of azimuths from 0° to 180°) on elongation estimates for the fault population at each study site. Assuming dip-slip motion for each individual fault, we computed the ratio between the apparent fault heave, h_{app}, at a given geographic azimuth (0–180°) and the total fault heave, h_{tot}, in the dip direction of that fault. Mathematically, this is the cosine of the angle between the dip direction and the azimuth in question. This individual heave ratio was averaged for all of the faults, both normal and reverse, in each analyzed population. This averaging method does not weigh each fault by total displacement but instead places equal weight on each fault in the population. This avoids the biases introduced by the few faults with large displacements whose orientation can significantly affect the results when weighted averages are used (as illustrated by the secondary dashed curve in Fig. 7c for the Lake San Antonio fault population).

Fig. 7b and c shows the results for the Williams Hill and Lake San Antonio fault population data sets, respectively. An ideal population of dip-slip faults, all striking perpendicular to the fold hinge, would produce a 100% average heave ratio (y-axis on Fig. 7a and b) parallel to the fold hinge (x-axis). Variations in fault orientations decrease the total possible average heave ratio and can shift the azimuth of maximum possible elongation away from the hinge. However, for both study sites the maximum heave ratio is achieved at azimuths nearly parallel to the local fold hinge. This implies that the fault populations are extremely well-oriented to accommodate hinge-parallel elongation (assuming dip-slip motion). Further, for the traverse orientations at Williams Hill (115°, 140°, and 150°), the estimated heave ratio is close to the maximum value. This suggests that the elongation estimates from Williams Hill discussed in Sections 4.2 and 4.3 represent reasonable estimates of the magnitude of hinge-parallel elongation for this site.

5. Kinematic modeling

5.1. Methodology

Assuming the data presented in Sections 3 and 4 provide a reasonable measure of finite strain, we estimate the deformation gradient tensor **F** (Malvern, 1969) responsible for the *en echelon* folds adjacent to the Rinconada fault. Note that **F** is the same as the deformation matrix **D** used to describe monoclinic transpression (Fossen and Tikoff, 1993; Tikoff and Fossen, 1993), which can be written as:

$$\mathbf{F} = \begin{bmatrix} 1 & \Gamma & 0 \\ 0 & k & 0 \\ 0 & 0 & k^{-1} \end{bmatrix} = \begin{bmatrix} 1 & \dfrac{\gamma(k-1)}{\ln(k)} & 0 \\ 0 & k & 0 \\ 0 & 0 & k^{-1} \end{bmatrix} \quad (1)$$

The coordinate system for **F** is defined such that the x-axis is parallel to the shear direction, the y-axis is normal to the shear plane, and the z-axis is vertical. The magnitude of contraction perpendicular to the shear plane is $1 - k$. The effective shear

strain parallel to the fault Γ, a function of both k and the true shear strain γ, is normalized over the width of the deforming zone. In monoclinic transpression, area loss occurs in the horizontal xy plane during deformation, but the vertical stretch k^{-1} directly compensates the contraction in the y-direction to preserve volume in the system. Thus, the 2×2 matrix in the upper left hand corner fully describes the deformation occurring in the xy plane where folding takes place.

The average orientation of folds for each study region (Section 3.2) provides the relative angle θ between the maximum horizontal finite strain axis and the shear direction. The elongation e documented from the fault traverses (Section 4) provides an estimate of the maximum horizontal stretch $(1+e)$, or S_{Hmax}, in the direction θ. These two known quantities can be used to solve the two unknowns, k and Γ, in $\mathbf{F}$ by solving equations for the eigensystem of $\mathbf{FF^T}$ (Tikoff and Fossen, 1993). This solution is non-unique, with two possible values for both k and Γ; we chose the solution where both k and Γ are positive and $k<1$, corresponding to transpression.

Once $\mathbf{F}$ is determined, and assuming deformation is steady-state, we can compute a variety of useful parameters to characterize deformation in the region. We solve for γ, using the value of Γ and k from Eq. (1), as well as the angle of oblique convergence α (Fossen et al., 1995) can be defined as:

$$\alpha = \tan^{-1}\left(\frac{\ln(k)}{\gamma}\right). \tag{2}$$

From the minimum horizontal eigenvalue and eigenvector of $\mathbf{FF^T}$, we can also find S_{Hmin}, the minimum horizontal stretch, a measure of shortening perpendicular to the fold hinges.

An alternative treatment of deformation decomposes $\mathbf{F}$ into distortional and rotational components (Elliott, 1972), where the rotational component, $\mathbf{R}$, is a matrix of the form:

$$\mathbf{R} = \begin{bmatrix} \cos\omega & -\sin\omega \\ \sin\omega & \cos\omega \end{bmatrix}. \tag{3}$$

Here, ω represents the vertical axis rotation in the system and can be written in terms of the components of $\mathbf{F}$ (corrected from the appendix of Tikoff and Fossen, 1993):

$$\omega = \tan^{-1}\left(\frac{\gamma(1-k)\ln(k)}{1+k}\right). \tag{4}$$

This rotation is caused by the wrench component of deformation (Lister and Williams, 1983) and should not be confused with the magnitude of fold hinge rotation. Instead, ω is used for comparison with independently derived estimates of vertical axis rotations from regional paleomagnetic data described (Section 6).

5.2. Results of kinematic modeling

The fold hinge orientation from maps (θ) and fault population analysis results (S_{Hmax}) were used to predict a range of α values responsible for distributed deformation at the two study sites assuming either active (Fig. 8a) or passive (Fig. 8b) fold rotation. This range was further narrowed by comparing α and θ values to predict maximum limb dips for each study area. The modeled limb dips provide an independent test of our approach since they can be compared with true limb dips observed in the field. Limb dip calculations were based on the geometric method presented by Jamison (1991) assuming active (Fig. 8c) or passive (Fig. 8d) fold rotation.

Other parameters from the kinematic modeling, including the values of k, Γ, γ, and ω, are reported in Table 3 assuming active rotation of fold hinges (see active versus passive discussion in Section 3.1). The total fault-parallel and fault-perpendicular displacements can be computed using a range of values for the deformation matrix $\mathbf{F}$, although it is first necessary to find the pre-deformation width of the zone (Horsman and Tikoff, 2005). The bold rows in the table represent our preferred estimates for deformation at each of the two study areas; the two bold rows for Lake San Antonio are due to different fold hinge orientations and limb dips at different distances from the fault. The results for each field area are discussed in more detail below.

5.2.1. Williams Hill

The average angle θ between fold hinges and the Rinconada fault from the Espinosa map (27°) is consistent with that of the local fold orientation near the fault traverses (25°). Orientations more than 5° from this average θ produce shortening and limb dip estimates that are incompatible with field data and are therefore not included in Fig. 8. For the fold hinge stretch, we tested a range of values based on elongation estimates from the fault population data between 1.04 and 1.06 (corresponding to $5 \pm 1°$ hinge-parallel elongation from fault population analysis).

Kinematic modeling predicts α values of 20–40° regardless of whether folds are treated as active or passive markers (Fig. 8a, b). Additionally, the model predicts 33–38° limb dips (Fig. 8c, d), in good agreement with the maximum limb dips of 30–40° from the original map (Dibblee, 1976). For the selected values shown in Table 3, the predicted rotation angles ω are 3–7°, shortening perpendicular to the fold hinges (from S_{Hmin}) is 16–38%, and shortening perpendicular to the Rinconada fault is 5–16%.

The current width of the folded zone adjacent to this segment of the Rinconada fault is ~21 km. Based on the results from kinematic modeling, we predict a range of original widths of between 22 and 25 km (corresponding to $k_{\max} = 0.95$ and $k_{\min} = 0.84$) implying 1–4 km of fault-perpendicular shortening. The magnitude of fault-parallel deformation corresponding to these widths varies from 2.3 to 5.5 km. Our preferred model (bold row in Table 3) suggests an original width of 23.5 km, with approximately 4.5 km of wrench deformation and 2.5 km of contraction.

5.2.2. Lake San Antonio

The fold patterns near Lake San Antonio are not consistent across the entire map area (Fig. 4b), requiring division of the map into two zones: (1) a 3-km wide, near-fault zone centered

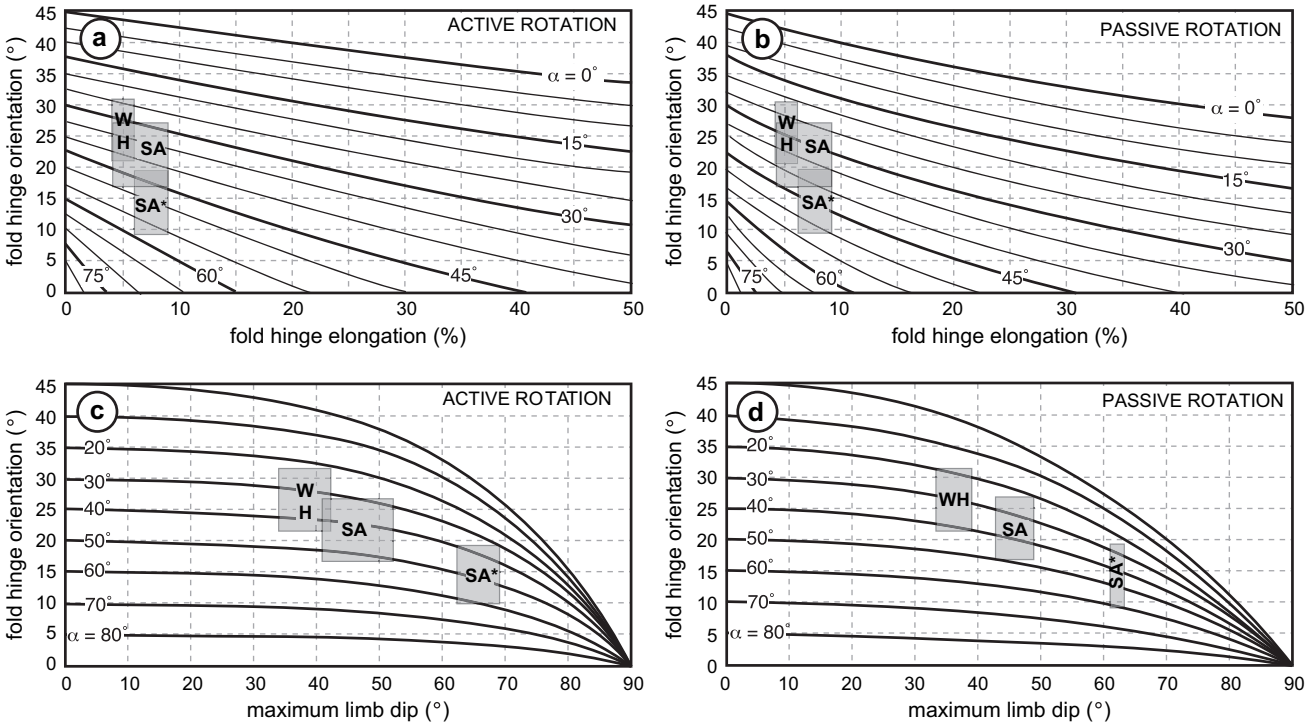

Fig. 8. Results of kinematic modeling of transpressional folding. The gray boxes on each chart represent the range of values for Williams Hill (WH) and Lake San Antonio (SA). The two boxes for Lake San Antonio reflect near-fault (SA*) and far-fault (SA) fold hinges. Graphs of fold hinge orientation versus fold hinge elongation show the range of α values predicted from the field data assuming (a) active and (b) passive fold rotations. Comparison of the α ranges from (a) and (b) with fold hinge orientations allows us to estimate the maximum limb dip expected for each region assuming (c) active and (d) passive fold rotations. This second set of charts serves as an independent test of our kinematic model since predicted limb dips can be compared to those measured in the field.

on the Rinconada fault including the acute fold hinges with steeper limb dips, and (2) a 15-km wide, far-fault zone southwest of the fault characterized by less acute fold hinges with moderate limb dips. This division does not necessarily suggest more rotation for near-fault folds but is more likely related to variations in strain partitioning across this region.

Our fault population data from Lake San Antonio are used to constrain the near-fault kinematic model. We use the average fold hinge obliquity within 2.5 km of the fault for θ (14°; Table 1), generally consistent with the local fold hinge orientation at the fault population site (10°). We tested a range of stretch values between 1.06 and 1.09 based on the fault population analysis at Lake San Antonio. For the far-fault kinematic model, we tested a range of fold orientations (20–24°; Table 1) and the range of elongations from our two fault population studies (1.04–1.09), since we have no field data to constrain elongation in this region. We recognize that the far-fault model is poorly constrained, although modeled limb dips can be used to refine the kinematic model results for this area.

Fig. 8 shows that near-fault (SA*) and far-fault (SA) parameters lead to distinctly different estimates of α (Fig. 8a, b) and limb dip (Fig. 8c, d) for these two regions. In the near-fault region, α is 30–60° with corresponding limb dips of 60–68°. The rotation ω varies from 6° to 16°, and shortening of the zone is 19–60% (Table 3). In the far-fault region, α is 25–50° (Fig. 8a, b) with limb dips of 36–60°. Rotation ω varies from 4° to 11° and shortening is 7–29%. Since ~35° model limb dips are most consistent with field data, elongation values should probably be ~1.04 for the far-fault region as indicated by the bold row in Table 3.

To compute the total fault-parallel and fault-perpendicular displacements for the San Marcos map area, we sum the bold values in Table 3 for the near-fault and far-fault zones. Our model predicts the near-fault zone, now 3 km wide, was originally 5.2 km wide (with 2.2 km of shortening) and accommodated 2 km of fault-parallel deformation. The far-fault zone, now 15 km wide, was 17 km wide, accommodating 2 km of shortening and 2.5 km of wrench motion. Together, the two zones at Lake San Antonio accommodated 4.5 km of wrench motion, consistent with the estimate from Williams Hill, and 4 km of shortening, slightly higher than that calculated for Williams Hill.

5.3. Comparison with previous models

The kinematic model derived here can be compared with other models for fold formation in oblique convergence. In particular, we can directly compare our model results from Williams Hill with models by Jamison (1991) and Krantz (1995) that were based on the fold map patterns from the Espinosa map (Fig. 4a; Dibblee, 1976).

Jamison's (1991) model used fold hinge orientation, fold shape (chevron or sinusoidal) and the maximum limb dip to quantify deformation recorded by *en echelon* folds. The inputs for the Espinosa segment included a mean fold

Table 3
Summary of input and output parameters for transpressional model of *en echelon* folding

Site	θ	S_{Hmax}	k	Γ	γ	α	ω	S_{Hmin}	limb dip	ISA_{Hmin}
Williams Hill	17	1.04	0.77	0.19	0.21	50	6	0.55	53	70
	17	1.06	0.72	0.26	0.30	47	9	0.46	58	69
	22	1.04	0.87	0.16	0.17	39	5	0.70	44	65
	22	1.06	0.84	0.22	0.24	37	7	0.62	48	64
	27	1.04	0.92	0.14	0.14	32	4	0.77	37	61
	27	**1.06**	**0.89**	**0.19**	**0.20**	**30**	**6**	**0.70**	**43**	**60**
	32	1.04	0.95	0.11	0.12	23	3	0.84	33	57
	32	1.06	0.94	0.16	0.17	21	5	0.78	36	56
	37	1.04	0.97	0.10	0.10	13	3	0.89	31	52
	37	1.06	0.97	0.14	0.14	12	4	0.84	32	51
Lake San Antonio	9	1.06	0.45	0.31	0.46	60	12	0.19	73	75
	9	1.09	0.40	0.40	0.61	56	16	0.14	75	73
	14	1.06	0.64	0.28	0.35	52	10	0.36	63	71
(near-fault)	**14**	**1.09**	**0.58**	**0.37**	**0.48**	**49**	**13**	**0.28**	**71**	**70**
	19	1.04	0.81	0.18	0.20	46	6	0.61	50	68
	19	1.06	0.76	0.24	0.28	44	8	0.52	55	67
	19	1.09	0.71	0.33	0.39	41	11	0.43	60	66
(far-fault)	**24**	**1.04**	**0.89**	**0.15**	**0.16**	**37**	**5**	**0.73**	**41**	**64**
	24	1.06	0.85	0.21	0.23	36	6	0.64	47	63
	24	1.09	0.81	0.29	0.32	33	9	0.56	53	62
	29	1.04	0.93	0.13	0.13	28	4	0.80	36	59
	29	1.06	0.90	0.18	0.19	27	5	0.74	42	59
	29	1.09	0.88	0.25	0.27	24	8	0.66	47	57

The inputs are: θ, orientation of the fold hinge relative to the bounding Rinconada fault; S_{Hmax}, the stretch along that fold hinge. The outputs include: k, the shortening in the direction perpendicular to the fault; Γ, the effective shear strain parallel to the fault; γ, the true shear strain parallel to the fault (i.e. simple shear component); α, the angle of oblique convergence; ω, the rotational component of the deformation matrix; S_{Hmin}, shortening perpendicular to fold hinges; limb dip, is the maximum limb dip assuming a sinusoidal fold shape (see Jamison, 1991); and ISA_{Hmax} is the inferred orientation of the maximum horizontal instantaneous stretching direction. Bold rows represent preferred model parameters for each site. See text for details.

orientation of 18° relative to the fault direction and maximum limb dips of 30–40°. Assuming a passive model of fold hinge rotation, these input values predicted maximum hinge-parallel elongations of 2.5–4.5%, shortening perpendicular to fold hinges of 7–14%, fault-parallel contraction of 6–12%, and an angle of oblique convergence of 50°. The disadvantages of this map-based model are two-fold. First, fold hinge rotation was treated as passive, which may overestimate the total deformation. Second, the average fold hinge orientation was computed by weighting each fold hinge equally and taking its average orientation along the whole hinge. These orientations were then compared with the average fault orientation for the map area (which varies by up to 20°). Our gridding technique for quantifying fold hinges produces a significantly different obliquity angle (27°) for the same map region.

Krantz (1995) treated folds as active markers during progressive deformation. His model also used 18° as the mean angle between folds and faults (taken from Jamison, 1991) and assumed a 45° angle of oblique convergence in order to achieve results comparable to those of Jamison (1991). This model predicted 7% hinge-parallel elongation and 32% shortening perpendicular to fold hinges. The disadvantage of this model is that one must assume an angle of oblique convergence in order to compute relevant values. Additionally, the mathematical computations are based on a deformation matrix that applies the pure shear and simple shear components sequentially (Sanderson and Marchini, 1984), which is only appropriate for finite deformation. Our analysis used a deformation matrix that allows simultaneous pure and simple shear (Tikoff and Fossen, 1993), making it possible to track the path of fold hinges through progressive deformation assuming steady-state conditions.

Our data, based on field measurements of hinge-parallel elongation and not solely on map patterns, compare favorably with both previous models despite their different assumptions. Our measured hinge-parallel elongation values of 4–6% fall between the ranges of their predicted values. The angle of oblique convergence that we obtain (20–40°), however, is lower than both of these models (45–50°), which has implications for the amount of strike-slip partitioning across the Rinconada fault system. This difference is mainly due to our gridding technique for quantifying fold hinge orientations (giving an average value of 27° and not 18°) on the Espinosa map. As discussed in Section 3.1, fold hinge orientation is the most sensitive indicator for predicting α (Fig. 3).

6. Paleomagnetism from the Rinconada fault system

6.1. Methodology

Our paleomagnetic study focused on samples from folded Tertiary sediments on either side of the Rinconada fault

without crossing any other major mapped sub-parallel faults (Fig. 1). We drilled 23 sites within siltstones, mudstones and dolostones of the Monterey Formation and three sites in sandstones of the Pancho Rico Formation. In previous paleomagnetic studies of the Monterey Formation, well-defined natural remnant magnetism was recorded in dolomites (Hornafius, 1985; Hornafius et al., 1986), where the primary remanence is generally carried by detrital magnetite (Hart and Fuller, 1988). Dolomitic shales and siliceous mudstones have also been shown to have a well-defined natural remanent magnetism that is able to record polarity reversals (Omarzai, 1996; Khan et al., 2001). The Pancho Rico Formation has not, to our knowledge, been used in prior paleomagnetic analyses.

Cores were oriented in the field with magnetic and sun compasses and cut into specimens in the laboratory. Samples were stored and measured in a magnetically shielded room, with a 350 nT low field environment useful for studying weakly magnetized sedimentary rocks. At least seven and up to 10 specimens were measured for each site in progressive thermal demagnetization step-heating experiments from 90 °C to at least 600 °C, in steps appropriate to the demagnetization pattern of the specimens. Alternating-field demagnetization was also used to study these rocks, but as in other studies of the Monterey Formation (e.g. Omarzai, 1996), we found that thermal demagnetization produced better results.

6.2. Results

6.2.1. Demagnetization behavior

The majority of specimens (111/126) had well-defined demagnetization behavior, yielding 22 sites with acceptable mean directions (Table 4). Reverse polarity was observed in 4 of the 22 sites indicating that our sampling procedure probably covered a time period long enough to average out secular variations.

Several typical demagnetization spectra are shown in Fig. 9. Many samples displayed a secondary component of remanent magnetization that was unblocked at low temperatures (<200 °C). This component was probably due to viscous remanent magnetization. The second-removed component, represented by a linear demagnetization path, was unblocked at moderate to high temperatures (300–550 °C). This magnetization component had either normal or reverse polarity directions.

6.2.2. Tilt test

A paleomagnetic tilt test for all of the sites in this study yields an inconclusive result, despite the clear presence of both normal and reverse polarity directions that are well-defined at the site level. We observe that all the reverse polarity sites, considered separately, pass the paleomagnetic tilt test (Fig. 10a), indicative of a pre-folding magnetization. Several

Table 4
Summary of data from paleomagnetic stations

Site	Latitude (°)	Longitude (°)	Rock type	Fm	Pmag code	Declination	Inclination	*n*/no	*k*	α95	Bedding	
											S	*D*
04Tm1	36.268	121.435	Siltstone	M	p	188	−22.9	7/7	175	4.6	107	31
04Tm2	36.268	121.435	Siltstone	M	r	9.6	52.9	5/5	21	17.2	114	29
04Tm3	36.268	121.435	Siltstone	M	p	193	−15.5	3/5	418	6	118	30
04Tm4a	36.268	121.435	Siltstone	M	r	7.9	61.4	3/3	60	16	106	79
04Tm4b	36.268	121.435	Siltstone	M	r	21.5	67.9	3/3	62	15.8	290	83
04Tm5	36.268	121.435	Siltstone	M	r	20.7	55.8	5/5	347	4.1	103	40
04Tm6	36.267	121.435	Siltstone	M	r	12.1	41.9	3/5	18	29.6	102	40
04Tm7	36.206	121.277	Siltstone	M	r	5.3	37.6	4/5	95	9.5	314	44
04Tm8	36.211	121.279	Siltstone	M	r	357.9	53.7	5/5	254	4.8	328	42
04Tm9	36.230	121.282	Siltstone	M	p	289.5	65.6	4/5	89	9.7	310	36
04Tm10	36.158	120.864	Sandstone	PR	r	347.7	51.2	8/8	16	14.3	305	30
04Tm11	36.171	120.850	Sandstone	PR	r	5.5	49.9	1/5	na	na	192	34
04Tm12	36.187	120.829	Sandstone	PR	ng			0/5				
04Tm13	36.237	121.283	Siltstone	M	ng			0/5				
04Tm14	36.231	121.281	Siltstone	M	r	359	51.4	6/6	214	4.6	294	31
04Tm15	36.234	121.282	Siltstone	M	ng			0/5				
04Tm16	35.776	120.889	Dolomite	M	p	163.1	−69.7	6/6	187	4.9	317	20
04Tm17	35.776	120.889	Dolomite	M	p	192.9	−45.8	6/6	226	4.5	146	17
04Tm18	35.764	120.885	Siltstone	M	p	4.3	65	6/6	8	28.5	286	13
04Tm19	35.764	120.885	Siltstone	M	r	21.6	52.3	3/4	15	33	265	40
04Tm20	35.856	121.056	Siltstone	M	p	23.6	50.7	6/6	140	5.7	200	22
04Tm21	35.855	121.056	Siltstone	M	p	14.2	53.9	6/6	115	6.3	278	9
04Tm22	35.855	121.056	Siltstone	M	r	8.2	51.1	6/6	152	5.5	308	22
04Tm23	35.855	121.056	Siltstone	M	p	16.1	62.1	6/6	108	6.5	335	17
04Tm24	35.767	120.886	Siltstone	M	ng			0/4				
04Tm25	35.987	121.012	Siltstone	M	p	358	58.7	7/7	196	4.3	158	2
04Tm26	35.987	121.012	Siltstone	M	p	15.5	54.7	6/6	45	10.1	166	5

Abbreviations as follows: Fm – formation with Monterey (M) or Pancho Rico (PR); pmag code: p – primary remanent magnetization, r – remagnitization; ng – no good; declination and inclination of the in situ Fisher mean; *n*/no – indicates the number of samples used out of the total possible to estimate paleopoles; *k* is the concentration parameter; α95 – indicates the 95% confidence ellipse size; bedding measurements of strike (*S*) and dip (*D*).

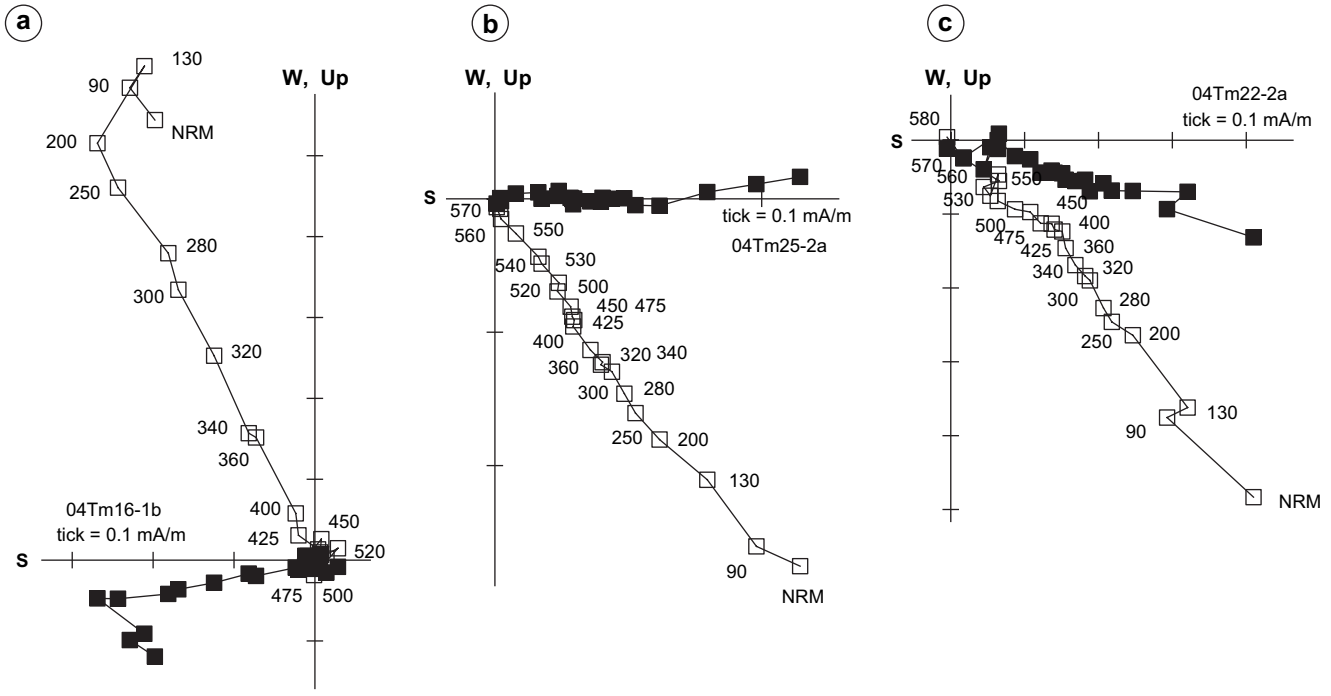

Fig. 9. Orthogonal vector plots of thermal demagnetization results. Filled symbols correspond to the horizontal vector component, open symbols to the vertical component projected onto the plane of the figure. Thermal demagnetization steps in C°. Plots show examples of (a) reverse polarity, primary magnetization, (b) normal-polarity primary magnetization, and (c) normal-polarity remagnetization.

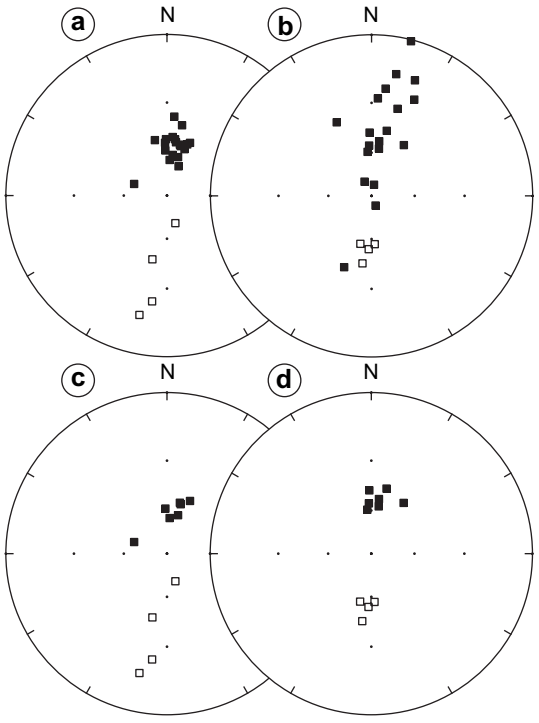

Fig. 10. Lower hemisphere, equal-angle stereographic projections of paleomagnetic site mean directions. Open symbols denote upper-hemisphere, filled lower-hemisphere. Projections show (a) all site means, in-situ and (b) tilt-corrected coordinates; (c) selected site means, in-situ and (d) tilt-corrected coordinates. Note that selected sites are well-clustered and antipodal following tilt-correction.

of the normal-polarity sites have tilt-corrected mean directions that are antipodal to the tilt-corrected directions of the reverse polarity sites (Fig. 10b). Using the subset of these 11 sites (all from the Monterey Formation) with both normal and reverse polarity site mean directions (Table 5), we show that the data pass the Tauxe and Watson (1994) paleomagnetic tilt test at 95% confidence, with maximum directional clustering occurring at 100% untilting (Fig. 11).

The remaining sites (11/26) have clearly defined directions that fail the paleomagnetic fold test, indicating that these rocks have been remagnetized. Because these rocks have not experienced significant heating, a fluid-induced origin for this remagnetization is more likely, as is proposed for many occurrences of remagnetized rocks in fold and thrust belts (McCabe and Elmore, 1989; McCabe and Channell, 1994; Stamatakos et al., 1996; Enkin et al., 2000). An investigation of the nature of this remagnetization will be presented elsewhere.

These results demonstrate that sites within the Monterey Formation retain an ancient, dual-polarity, pre-folding magnetization. Compared with a Miocene expected direction (10 Ma North American reference pole of Besse and Courtillot, 2002), a clockwise rotation of $13.6 \pm 7^{\circ}$ relative to North America, since the Miocene, is indicated.

6.3. Comparison with other regional paleomagnetic data

Regional paleomagnetic studies have often used Miocene-age rocks, including the Monterey Formation, to document the magnitude of vertical axis rotations of tectonic blocks in

Table 5
Average paleomagnetic data from sites with primary remanent magnetization

Group Means	declin.	inclin.	*N*	*k*	$\alpha 95$
rev, in situ	187.9	−38.6	4	10.0	30.5
rec, tilt-correct	185.2	−52.7	4	130.1	8.1
normal, in situ	5.4	61.4	7	27.7	11.7
normal, tilt-correct	8.1	52.7	7	71.4	7.2
combined, in situ	6.6	53.4	11	14.2	12.6
combined, tilt correct	7.0	52.7	11	92.3	4.8

Abbreviations same as in Table 4. *N* stands for the number of site averages used for each calculation.

the deforming plate boundary system. Large (>90°) clockwise rotations were determined for many sites in the Transverse Ranges (e.g. Hornafius, 1985; Luyendyk et al., 1985; Luyendyk, 1991) south of the Rinconada and Big Pine faults. In contrast, sites immediately north of the Big Pine fault show conflicting declination anomalies with both small (<10°) counterclockwise (e.g. Terres and Luyendyk, 1985) and clockwise rotations up to 25° (Ellis et al., 1993; Onderdonk, 2005) for Tertiary sedimentary and igneous rocks. Paleomagnetic studies along the coast, on Miocene-age and older rocks, demonstrate 40–50° clockwise rotations (Greenhaus and Cox, 1979, Horns and Verosub, 1995; Khan et al., 2001), significantly greater than those from inland sites.

Closer to our study region, Omarzai (1996) documented a $14.4 \pm 5°$ clockwise rotation from the Monterey Formation near Greenfield (Fig. 1). This rotation was computed relative to the Irving (1979) 20 Ma Miocene paleopole and was not interpreted conclusively as a declination anomaly (Omarzai, 1996), since nearby pilot studies showed no evidence for vertical axis rotations (Coe et al., 1984). We recomputed the vertical axis rotation from this study using the newer 10 Ma Miocene pole (Besse and Courtillot, 2002), and found $17 \pm 5°$ rotation, similar within error to our $13.6 \pm 7°$ rotation. The consistency between these two data sets suggests that the region adjacent to the Rinconada fault has rotated ~15° since the Late Miocene.

7. Integrating kinematic modeling and paleomagnetic data

The bulk rotation estimates from kinematic modeling of *en echelon* folds, which range from 3° to 16° (ω in Table 3), overlap with the paleomagnetically derived vertical axis rotation of $14 \pm 7°$. These data sets are independently derived and together constrain the hypothesis of distributed wrench deformation adjacent to the Rinconada fault.

To better illustrate the relation between these data sets, we reanalyzed a transpressional folding experiment from Tikoff and Peterson (1998) in Fig. 12. In this example, *en echelon* folds developed under transpressional boundary conditions ($\alpha = 45°$). Using the average hinge orientation and the stretch perpendicular to the fold hinges (S_{Hmin}) predicts that $\alpha = 46°$, consistent with the imposed deformation, and $\omega = 8°$ clockwise (Fig. 12c). This style of analysis is similar to our approach using fold orientations, stretch estimates from fault populations, and kinematic modeling of *en echelon* folds adjacent to the Rinconada fault.

The grid superimposed onto the analogue model also records the distortion and rotation due to transpressional deformation (Fig. 12b). We determined **F** (Eq. (1)) from the displacement between the initial and final states of each grid box; no assumption of transpression was required for these calculations. Unlike the fold hinges, which are best developed in the center of the model, deformation of the grid is recorded continuously across the entire system. Distinct variations are observed (lines closer together in center) that are mostly likely a result of boundary effects. In the central region, kinematic modeling predicts that α is $37 \pm 20°$ and ω is $9 \pm 6°$, and for the margins, α is $19 \pm 40°$ and ω is $3 \pm 23°$. This analysis, which uses displacements to characterize deformation in small areas across the grid, is similar to the regional paleomagnetic measurements. Each individual grid box is analogous to a paleomagnetic site. The large error bars of ω reflect the natural variation in the system (Fig. 12d).

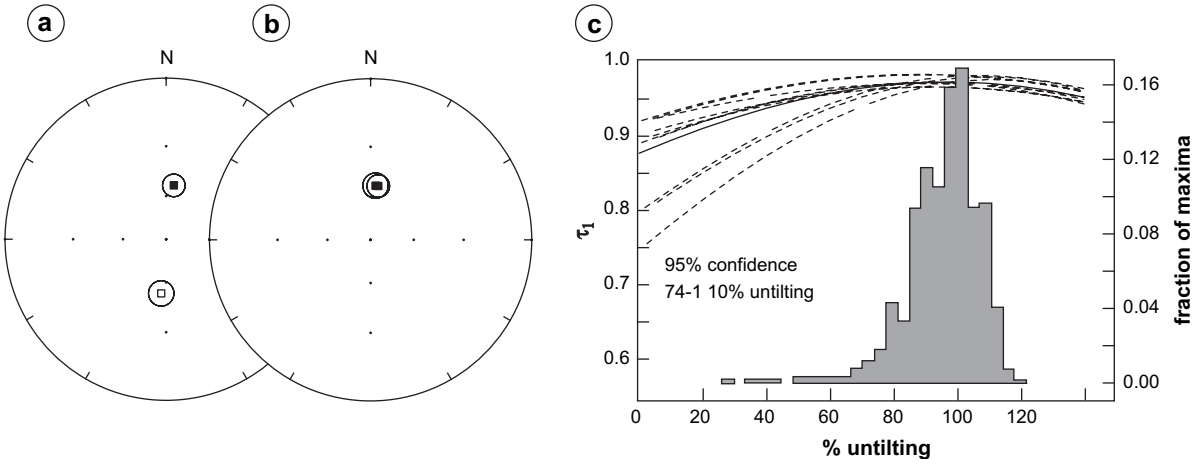

Fig. 11. Paleomagnetic group mean directions with 95% confidence radii. Equal area projections show (a) 100% tilt-corrected normal and reverse polarity means, (b) reverse-polarity mean inverted, demonstrating a positive paleomagnetic reversals test for these data. Graph in (c) demonstrates results of Tauxe and Watson (1994) paleomagnetic tilt test for the selected site means. The results indicate peak in directional clustering at 100% untilting, and that the tilt test is positive.

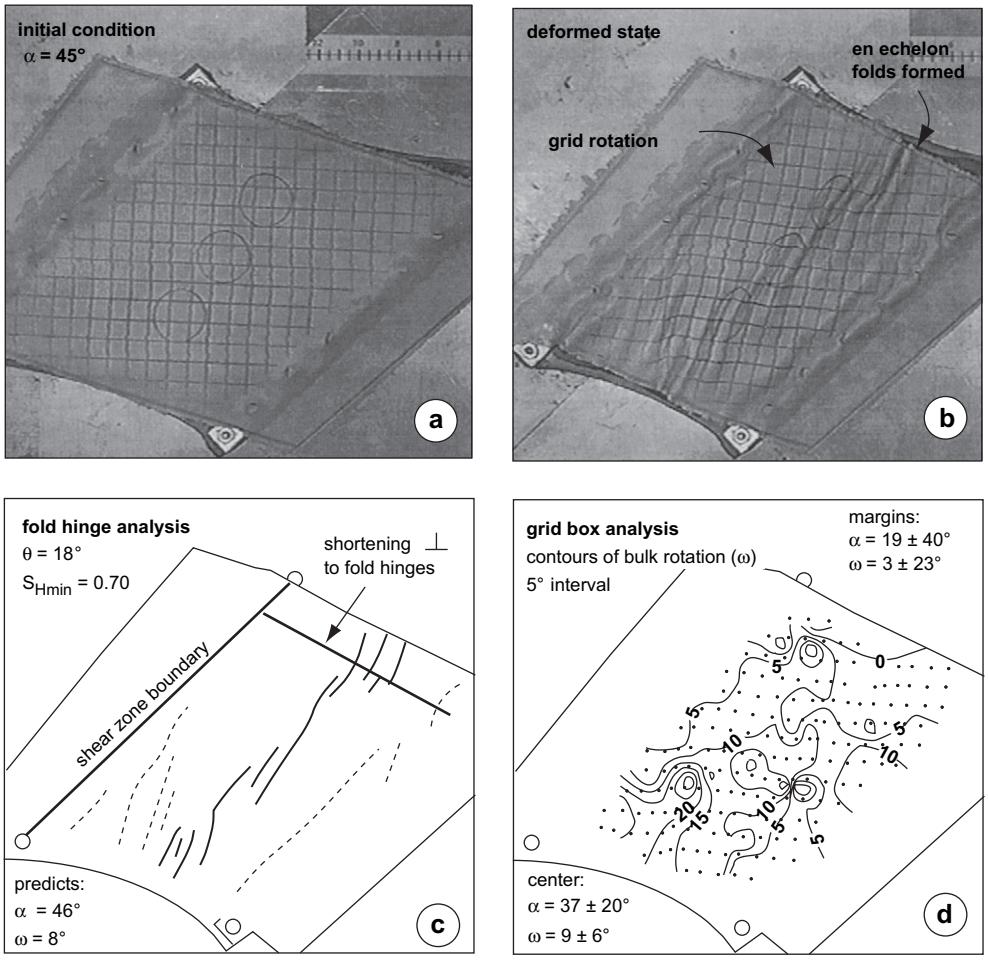

Fig. 12. Example of transpressional folding experiment from Tikoff and Peterson (1998). Photographs of (a) the initial state with $\alpha = 45°$ and (b) the deformed state. (c) Cartoon showing the fold hinges used for characterizing deformation using a method similar to our kinematic fold modeling for the Rinconada fault. (d) Cartoon showing a contour map of ω values, computed from each grid box, with a contour interval of 5°. This grid-based method has greater variations across the deforming zone and is analogous to paleomagnetic sampling adjacent to the Rinconada fault. Values of α and ω are reported for both analyses. See text for details.

To summarize, vertical axis rotation, easily observable in our example by the grid rotation (Fig. 12), is an inevitable consequence of transpression due to the wrench component of deformation. Because the $14 \pm 7°$ vertical axis rotation from our paleomagnetic data is consistent with the rotation derived from kinematic modeling of *en echelon* folds, we have independent confirmation of a component of distributed wrench deformation adjacent to the Rinconada fault. Although paleomagnetic declination anomalies in strike-slip systems are often interpreted as rigid block rotations (e.g. McKenzie and Jackson, 1983; McKenzie et al., 1986; Lamb, 1987; Dickinson, 1996), we attribute much of the vertical axis rotation recorded by our paleomagnetic analyses in central California to internal deformation of the rocks adjacent to the Rinconada fault.

8. Discussion

8.1. Deformation rates and strike-slip partitioning of the Rinconada fault system

Our kinematic model assumes that *en echelon* folds adjacent to the Rinconada fault formed in monoclinic transpression. The model results from Williams Hill and Lake San Antonio are generally consistent (although those from Williams Hill are better constrained), suggesting that deformation magnitude and style are generally similar along strike. Based on the data from these sites, we estimate that *en echelon* folds within 10 km of the Rinconada fault accommodated ~5 km of wrench deformation and 2–4 km of shortening.

Bracketing the onset of deformation between 6 and 8 Ma (maximum) and 3.5 Ma (minimum) suggests wrench deformation rates of 0.6–1.4 mm/yr and shortening rates of 0.3–1.1 mm/yr. For comparison, the present fault-parallel deformation rate for the San Andreas fault system is 39 ± 2 mm/yr (Argus and Gordon, 2001), suggesting that these *en echelon* folds may accommodate up to 3% of the wrench component of plate motion. The estimate for shortening at this latitude is approximately 3.5 ± 1.2 mm/yr (from profile $D - D'$ in Argus and Gordon, 2001), suggesting that distributed deformation adjacent to the Rinconada fault may account for up to 30% of the total contraction across the 180-km wide system.

A useful comparison can also be made between the distributed and discrete components of deformation for the Rinconada

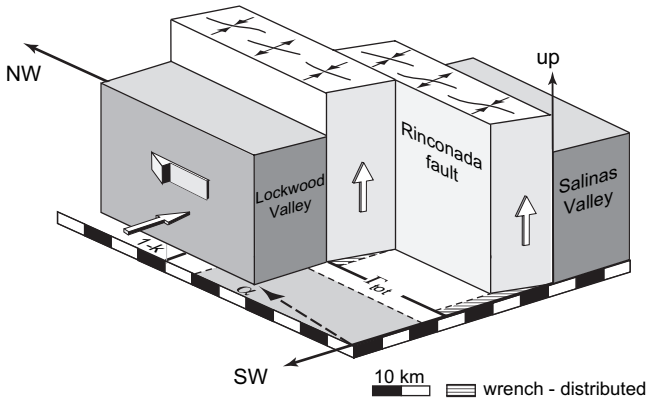

Fig. 13. Cartoon showing the combined discrete and distributed deformations accommodated by the Rinconada fault system since the Pliocene. The horizontal components of deformation are scaled; the vertical is not. The wrench component of deformation is broken into discrete (white) and distributed (striped) displacements. The Salinas and Lockwood Valleys are shown here as rigid blocks, although deformation in these areas remains uninvestigated.

fault system (Fig. 13). Folded Pliocene-age sediments were offset 18 km on the Rinconada fault (Durham, 1965a). Integrating this offset with our kinematic fold modeling suggests that 22% of the wrench component of deformation (5 km of the 23 km total regional offset) is due to distributed deformation. Alternatively stated, the Rinconada fault system is ~80% strike-slip partitioned. The contraction estimate of 2–4 km, combined with the total wrench deformation of 23 km, can be used to estimate the local angle of oblique convergence for the Rinconada fault system (Eq. (2)). Depending on the value of k chosen, α may vary from 3° ($k = 0.95$) to 10° ($k = 0.85$), consistent with the 5° angle of oblique convergence for the entire San Andreas fault system (e.g. Argus and Gordon, 2001).

8.2. Kinematic modeling using en echelon folds

Our results are broadly similar to those from other regional kinematic models (Jamison, 1991; Krantz, 1995), but our approach has several important advantages. First, measurements of fold hinge orientations using a grid analysis better quantify the variability in fold hinge length and strike across the study area. Since longer fold hinges may reflect the coalescence of early formed folds (Ghosh and Ramberg, 1968), the ability to measure the changing orientations is important for the analysis of regional strain. This factor is the major reason why our model predicts lower angles of oblique convergence for regions adjacent to the Rinconada fault than other kinematic models (Jamison, 1991; Krantz, 1995). Second, estimates of hinge-parallel elongation are derived from field measurements of fault populations and not solely based on map patterns of folding. Detailed analysis of fault populations allowed quantification of elongation magnitude and orientation; the maximum elongation was found to be parallel to the local fold hinges. Third, regardless of whether fold hinges are treated as active or passive markers during progressive deformation, very similar angles of oblique convergence are found. Fourth, integration of the discrete and distributed components of deformation since the Pliocene for the Rinconada fault predicts α from 3° to 10°, consistent with the 5° bulk plate motion direction for the entire San Andreas fault system (Argus and Gordon, 2001). Last, the wrench component of deformation causes a 3–16° rotation in the system. This rotation was confirmed by the independently derived $14 \pm 7°$ vertical axis rotation from paleomagnetic data.

8.3. Implications of distributed fault-parallel deformation

This kinematic analysis of the Rinconada fault system can be treated as a case study of deformation patterns within the broader San Andreas fault system. Folding is common in Tertiary and older sedimentary rocks along the fault system in central California (Jennings et al., 1977). Young folds are sometimes expressed in the local topography (e.g. Kettleman and Lost Hills) and often form structural traps like those in oil-fields in the San Joaquin Valley (e.g. Harding, 1973, 1976).

In some areas, fold hinges are nearly parallel to the San Andreas fault (e.g. Jennings et al., 1977), perhaps suggesting that little wrench deformation is accommodated in these regions (Mount and Suppe, 1987; Zoback et al., 1987). In other areas, however, fold hinges are oblique to the fault with the consistent stepping relationships indicative of *en echelon* folds (e.g. Miller, 1998). These folded regions, similar to those adjacent to the Rinconada fault, may record a significant component of distributed wrench deformation that should not be overlooked when studying the San Andreas fault system as a whole. Detailed structural and paleomagnetic investigations are necessary to help refine our understanding of strain partitioning across the plate boundary system.

9. Conclusions

Using a field- and map-based approach, we quantified the distributed component of deformation adjacent to the Rinconada fault using *en echelon* folds at Williams Hill and Lake San Antonio. Fold hinge orientations are 27° and 14° oblique to the Rinconada fault at these sites, respectively. Fault population analysis reveals maximum horizontal elongation of 4–9% in a direction parallel to the major fold hinges. These data are used to estimate the orientation and stretch, respectively, of the maximum horizontal finite strain axis that is then used to construct a kinematic model for regional distributed deformation. Our model assumes that folding occurred in monoclinic transpression and that fold hinges behave as finite strain markers (active rotation).

The model results indicate an effective angle of oblique convergence of 20–50° for the folded region adjacent to the Rinconada fault, implying that a significant wrench component of deformation is accommodated through folding. The 3–16° rotation predicted by our kinematic model is consistent with the independently derived $14 \pm 7°$ vertical axis rotation indicated by paleomagnetic analyses throughout the region. We estimate the magnitude of fault-parallel and fault-perpendicular components of deformation for a 20-km wide region adjacent

to the Rinconada fault to be 5 km and 2–4 km, respectively. Depending on timing for the onset of deformation, these offsets suggest a 0.6–1.4 mm/yr fault-parallel deformation rate and a 0.3–1.1 mm/yr fault-perpendicular rate. Integration of discrete and distributed deformation for the Rinconada fault suggests a regional 3–10° angle of oblique convergence, consistent with the bulk plate motion direction for the San Andreas fault system, and 80% strike-slip partitioning since the Pliocene.

Acknowledgements

We thank Scott Giorgis, Christopher Gordon, Skylar Primm and Bill Titus for their assistance in the field. Joshua Davis and Eric Horsman are thanked for innumerable invaluable discussions during the course of this research. The detailed comments of Nicola DePaola and John Waldron were helpful for improving the clarity of this manuscript. This material is based upon work supported under a National Science Foundation Graduate Research Fellowship (Titus) and supported by NSF-EAR0208038 (Housen and Tikoff).

Appendix A. Data from fault traverses

Fault #	Distance (cm)	Fault orientation				ΔL dip dir (cm)	ΔL traverse (cm)
		Dip dir	Dip	Sense	Separation (cm)		
Traverse 1							
0	0	345	77	N	200	–	–
1	457	163	82	R	38	5.3	3.5
2	838	150	57	N	142	77.5	63.5
3	1600	175	85	N	25	2.2	1.1
4	2210	265	83	N	13	1.5	1.3
5	2362	115	40	N	64	48.6	48.6
6	2514	100	72	N	25	7.8	7.6
7	2514	95	72	N	51	15.7	14.8
8	2819	115	62	N	200	93.9	93.9
9	3429	130	28	N	200	176.6	170.6
10	4343	135	23	N	3	2.3	2.2
11	7543	125	33	N	152	127.8	125.9
12	9982	120	5	N	13	12.7	12.6
13	12 420	130	20	N	13	11.9	11.5
14	12 725	105	90	SSD	64	–	–
15	13 639	98	90	SSU	75	–	–
16	14 401	125	34	N	4	3.2	3.1
17	14 706	305	30	N	25	22	21.7
18	14 706	148	65	N	250	105.7	88.6
19	15 011	105	50	N	75	48.2	47.5
20	16 230	80	81	N	13	2	1.6
21	18 059	288	45	N	33	23.3	23.2
22	18 059	85	85	R	114	10	8.6
23	20 302	95	56	N	75	41.9	39.4
24	20 722	155	55	N	50	28.7	22
25	21 283	310	68	N	13	4.8	4.6
26	21 564	330	67	N	25	9.9	8.1
27	22 405	320	48	N	200	133.8	121.3
28	23 456	0	85	N	5	0.4	0.2
29	23 456	140	15	N	5	4.9	4.4
30	23 456	120	65	N	13	5.4	5.3
31	23 456	105	70	R	8	2.6	2.6
32	23 456	105	68	N	13	4.8	4.7
33	23 456	42	79	R	50	9.5	2.8
34	25 980	55	30	N	75	65	32.5
35	29 485	261	30	N	75	65	53.8
xx	31 027	160	28	N	0	–	–
					Total ΔL	1148	1036
					Extension		3.5
Traverse 2							
0	0	6	20	N	11.4	–	–
1	0	110	59	N	14	7.2	6.2
2	701	104	29	N	33	28.9	23.4
3	911	334	20	R	10.2	9.5	9.3
4	1892	110	37	N	25.4	20.3	17.6
5	5187	156	46	N	7.6	5.3	5.1
6	5888	351	25	N	5.1	4.6	3.9
7	6028	317	34	N	304.8	252.7	252.3
8	6729	350	30	N	7.6	6.6	5.7
9	7711	108	55	N	57.2	32.8	27.8
10	7711	352	32	N	44.5	37.7	32
11	8271	32	68	N	7.6	2.9	0.9
12	8552	272	90	N	76.2	0	0
13	8552	151	45	N	20.3	14.4	14.1
14	8622	327	23	N	22.9	21	20.9
15	8902	82	63	N	30.5	13.8	7.3
xx	10 795	288	79	N	45.7	–	–
					Total ΔL	448	417
					Extension		4.0
Traverse 3							
0	0	341	25	N	5.1	–	–
1	561	89	36	N	15.2	12.3	5
2	771	323	15	N	6.4	6.1	6
3	2033	305	30	N	3.8	3.3	2.9
4	5538	326	42	N	22.9	17	16.8
5	9744	251	30	N	30.5	26.4	2.8
6	9744	137	45	N	10.2	7.2	6.8
7	9464	352	38	N	10.2	8	7.7
8	9744	121	78	N	3.8	0.8	0.7
9	10 165	162	68	N	6.4	2.4	2.4
10	10 165	127	28	N	5.1	4.5	4
11	10 515	329	40	N	5.1	3.9	3.9
12	12 268	121	25	N	25.4	23	19.1
13	12 268	333	28	N	15.2	13.5	13.4
14	12 478	335	38	N	33	26	26
15	13 529	315	30	N	5.1	4.4	4.1
16	14 090	340	25	N	50.8	46	45.9
xx	17 245	330	32	N	3.8	–	–
					Total ΔL	205	167
					Extension		1.0
Traverse 4							
0	0	145	65	N	0	–	–
1	600	98	10	N	400	393.9	365.2
2	2200	154	78	N	200	41.6	34.5
3	2350	131	71	N	20	6.5	6.4
4	2350	0	85	N	10	0.9	0.4
5	2700	336	85	N	20	1.7	1.4
6	3100	345	90	N	50	0	0
7	5900	338	87	N	20	1	0.8
8	5900	108	42	N	200	148.6	145.4
9	5900	96	46	N	200	138.9	126.9

(*continued on next page*)

(*continued*)

Fault #	Distance (cm)	Fault orientation				ΔL dip dir (cm)	ΔL traverse (cm)
		Dip dir	Dip	Sense	Separation (cm)		
10	6400	55	78	N	60	12.5	5.3
11	6500	43	78	N	80	16.6	3.7
12	8400	98	65	N	50	21.1	19.6
13	10 700	101	62	N	100	46.9	44.4
xx	12 600	130	90	N	10	–	–
					Total ΔL	830	754
					Extension		6.4
Small faults							
0	0	79	64	N	7	–	–
1	41	116	59	N	4.5	2.3	2.3
2	63	113	75	N	2	0.5	0.5
3	82	293	45	N	6.5	4.6	4.6
4	90	113	64	N	1.5	0.7	0.7
5	91	104	66	N	1.5	0.6	0.6
6	108	118	86	N	1.5	0.1	0.1
7	130	111	81	N	2	0.3	0.3
8	147	351	84	N	2.5	0.3	0.1
xx	160	145	52	N	4.5	–	–
					Total ΔL	9.4	9.2
					Extension		6.1

References

Argus, D.F., Gordon, R.G., 2001. Present tectonic motion across the Coast Ranges and San Andreas fault system in central California. Geological Society of America Bulletin 113, 1580–1592.

Atwater, T., Stock, J., 1998. Pacific-North America plate tectonics of the Neogene southwestern United States: an update. International Geology Review 40, 375–402.

Besse, J., Courtillot, V., 2002. Apparent and true polar wander and the geometry of the geomagnetic field over the last 200 Myr. Journal of Geophysical Research 107 (B11), 2300, doi:10.1029/2000JB000050.

Blake Jr., M.C., Campbell, R.H., Dibblee Jr., T.W., Howell, D.G., Nilsen, T.H., Normark, W.R., Vedder, J.G., Silver, E.A., 1978. Neogene basin formation in relation to plate tectonic evolution of San Andreas fault system, California. American Association of Petroleum Geologists Bulletin 62, 344–372.

Compton, R.R., 1966. Analyses of Pliocene–Pleistocene deformation and stresses in northern Santa Lucia Range, California. Geological Society of America Bulletin 77, 1361–1379.

Coe, R.S., Mertz Jr., K.A., Pettit, R.L., 1984. Paleomagnetic results from dolomite rocks of the Monterey Formation, Arroyo Seco area, California: dolomites of the Monterey Formation and other organic-rich units. Field Trip Guidebook – Pacific Section. Society of Economic Paleontologists and Mineralogists 41, 215.

Cox, A., Engebretson, D.C., 1985. Change in motion of Pacific plate at 5 Myr BP. Nature 313, 472–474.

Dewey, J.F., Holdsworth, R.E., Strachan, R.A., 1998. Transpression and transtension zones: continental transpressional and transtensional tectonics. Geological Society Special Publications, vol. 135, pp. 1–14.

Dholakia, S.K., Aydin, A., Pollard, D.D., Zoback, M.D., 1998. Fault-controlled hydrocarbon pathways in the Monterey Formation, California. American Association of Petroleum Geologists Bulletin 82, 1551–1574.

Dibblee, T.W., Jr., 1976. The Rinconada and Related Faults in the Southern Coast Ranges, California, and Their Tectonic Significance. U.S. Geological Survey Professional Paper 981.

Dickinson, W.R., 1996. Kinematics of transrotational tectonism in the California Transverse Ranges and its contribution to cumulative slip along the San Andreas transform fault system. The Geological Society of America Special paper 305, p. 46.

Ducea, M., House, M.A., Kidder, S., 2003. Late cenozoic denudation and uplift rates in the Santa Lucia Mountains, California. Geology 31, 139–142.

Durham, D.L., 1964. Geology of the Cosio Knob and Espinosa Canyon Quadrangles, Monterey County, California. U.S. Geological Survey Report B 1161-H, pp. 1–29.

Durham, D.L., 1965a. Evidence of Large Strike-slip Displacement along a Fault in the Southern Salinas Valley, California. U.S. Geological Survey Report P 0525-D, pp. 106–111.

Durham, D.L., 1965b. Geology of the Jolon and Williams Hill Quadrangles, Monterey County, California. U.S. Geological Survey Report B 1181-Q, pp. 1–27.

Durham, D.L., 1968. Geology of the Tierra Redonda Mountain and Bradley quadrangles, Monterey and San Luis Obispo Counties, California. U.S. Geological Survey Report B 1255.

Durham, D.L., Addicott, W.O., 1965. Pancho Rico Formation, Salinas Valley, California. U.S. Geological Survey Report P 0524-A, pp. 1–22.

Elliott, D., 1972. Deformation paths in structural geology. Geological Society of America Bulletin 83, 2621–2638.

Ellis, B.J., Levi, S., Yeats, R.S., 1993. Magnetic stratigraphy of the Morales Formation: late Neogene clockwise rotation and compression in the Cuyama basin, California coast ranges. Tectonics 12, 1170–1179.

Enkin, R.J., Osadetz, K.G., Baker, J., Kisilevsky, D., 2000. Orogenic remagnetizations in the front ranges and inner foothills of the southern Canadian Cordillera: chemical harbinger and thermal handmaiden of Cordilleran deformation. Geological Society of America Bulletin 112, 929–942.

Fossen, H., Tikoff, B., 1993. The deformation matrix for simultaneous simple shearing, pure shearing and volume change, and its application to transpression–transtension tectonics. Journal of Structural Geology 15, 413–422.

Fossen, H., Tikoff, B., Teyssier, C., 1995. Strain modeling of transpressional and transtensional deformation. Norsk Geologisk Tidsskrift 74, 134–145.

Galehouse, J.S., 1967. Provenance and paleocurrents of the Paso Robles formation, California. Geological Society of America Bulletin 78, 951–978.

Ghosh, S.K., Ramberg, H., 1968. Buckling experiments on intersecting fold patterns. Tectonophysics 5, 89–105.

Graham, R.H., 1978. Wrench faults, arcuate fold patterns and deformation in the southern French Alps. Proceedings of the Geologists' Association 89, 125–142.

Greenhaus, M.R., Cox, A., 1979. Paleomagnetism of the Morro Rock–Islay Hill complex as evidence for crustal block rotations in central coastal California: fault mechanics. Journal of Geophysical Research 84, 2393–2400.

Gross, M.R., Engelder, T., 1995. Strain accommodated by brittle failure in adjacent units of the Monterey Formation, U.S.A.: scale effects and evidence for uniform displacement boundary conditions. Journal of Structural Geology 17, 1303–1318.

Harbert, W., 1991. Late Neogene relative motions of the Pacific and North America plates. Tectonics 10, 1–15.

Harding, T.P., 1973. Newport-Inglewood trend, California: an example of wrenching style of deformation. American Association of Petroleum Geologists Bulletin 57, 97–116.

Harding, T.P., 1976. Tectonic significance and hydrocarbon trapping consequences of sequential folding synchronous with San Andreas faulting, San Joaquin Valley, California. American Association of Petroleum Geologists Bulletin 60, 356–378.

Harland, W.B., 1971. Tectonic transpression in Caledonian Spitsbergen. Geological Magazine 108, 27–41.

Hart, M., Fuller, M., 1988. Magnetization of a dolomite bed in the Monterey Formation: implications for diagenesis. Special section on rock magnetism. Geophysical Research Letters 15, 491–494.

Hornafius, J.S., 1985. Neogene tectonic rotation of the Santa Ynez Range, western Transverse Ranges, California, suggested by paleomagnetic investigation of the Monterey Formation. Journal of Geophysical Research 90, 12503–12522.

Hornafius, J.S., Luyendyk, B.P., Terres, R.R., Kamerling, M.J., 1986. Timing and extent of Neogene tectonic rotation in the western Transverse Ranges, California. Geological Society of America Bulletin 97, 1476–1487.

Horns, D., Verosub, K.L., 1995. Paleomagnetic investigation of late Neogene vertical axis rotation and remagnetization in central coastal California. Journal of Geophysical Research 100, 3873–3884.

Horsman, E., Tikoff, B., 2005. Quantifying simultaneous discrete and distributed deformation: fabric, strain and structural development in three dimensions. Journal of Structural Geology 27, 1168–1189.

Ingle, J.C., 1981. Origin of Neogene diatomites around the North Pacific rim: the Monterey Formation and related siliceous rocks of California. Society of Economic Paleontologists and Mineralogists. Pacific section.

Irving, E., 1979. Paleopoles and paleolatitudes of North America and speculations about displaced terrains: Geodynamics Canada. Canadian Journal of Earth Sciences 16, 669–694.

Isaacs, C.M., 1980. Diagenesis in the Monterey Formation Examined Laterally along the Coast Near Santa Barbara, California. Ph.D. thesis, Stanford University.

James, A.I., Watkinson, A.J., 1994. Initiation of folding and boudinage in wrench shear and transpression. Journal of Structural Geology 16, 883–893.

Jamison, W.R., 1991. Kinematics of compressional fold development in convergent wrench terranes. Tectonophysics 190, 209–232.

Jennings, C.W., Strand, R.G., Rogers, T.H., 1977. Geologic map of California: United States. California Division of Mines and Geology. scale 1:75,000.

Jones, R.R., Holdsworth, R.E., Clegg, P., McCaffrey, K., Tavarnelli, E., 2004. Inclined transpression. Journal of Structural Geology 26, 1531–1548.

Jones, R.R., Tanner, P.W.G., 1995. Strain partitioning in transpression zones. Journal of Structural Geology 17, 793–802.

Khan, S.O., Coe, R.S., Barron, J.A., 2001. Paleomagnetism of the middle–upper Miocene Monterey Formation, shell beach, Pismo basin: implications for the age and origin of the Monterey and tectonic block rotation in central coastal California. In: Magnetic Stratigraphy of the Pacific Coast Cenozoic. Society of Economic Paleontologists and Mineralogists, Pacific section 91, pp. 302–334.

King, G., Cisternas, A., 1991. Geological faulting: do little things matter? Nature 351, 350.

Krantz, R.W., 1995. The transpressional strain model applied to strike-slip, oblique-convergent and oblique-divergent deformation. Journal of Structural Geology 17, 1125–1137.

Lamb, S.H., 1987. A model for tectonic rotations about a vertical axis. Earth and Planetary Science Letters 84, 75–86.

Lin, S., Jiang, D., Williams, P.F., 1998. Transpression (or transtension) zones of triclinic symmetry: natural example and theoretical modeling. In: Continental Transpressional And Transtensional Tectonics. Geological Society Special Publications, vol. 135, pp. 41–57.

Lister, G.S., Williams, P.F., 1983. The partitioning of deformation in flowing rock masses. Tectonophysics 92, 1–33.

Little, T.A., 1992. Development of wrench folds along the Border Ranges fault system, southern Alaska. U.S.A. Journal of Structural Geology 14, 343–359.

Luyendyk, B.P., 1991. A model for Neogene crustal rotations, transtension and transpression in southern California. Geological Society of America Bulletin 103, 1528–1536.

Luyendyk, B.P., Kamerling, M.J., Terres, R.R., Hornafius, J.S., 1985. Simple shear of Southern California during Neogene time suggested by paleomagnetic declinations. Journal of Geophysical Research 90, 12454–12466.

Malvern, L.E., 1969. Introduction to the mechanics of a continuous medium. Prentice Hall, Inc., Englewood Cliffs, NJ.

Marrett, R., Allmendinger, R.W., 1991. Estimates of strain due to brittle faulting; sampling of fault populations. Journal of Structural Geology 13, 735–738.

Marrett, R., Allmendinger, R.W., 1992. Amount of extension on "small" faults: an example from the Viking Graben. Geology 20, 47–50.

McCabe, C., Channell, J.E.T., 1994. Late Paleozoic remagnetization in limestones of the Craven basin (northern England) and the rock magnetic fingerprint of remagnetized sedimentary carbonates. Journal of Geophysical Research 99, 4603–4612.

McCabe, C., Elmore, R.D., 1989. The occurrence and origin of late Paleozoic remagnetization in the sedimentary rocks of North America. Reviews of Geophysics 27, 471–494.

McKenzie, D., Jackson, J., 1983. The relationship between strain rates, crustal thickening, palaeomagnetism, finite strain and fault movements within a deforming zone. Earth and Planetary Science Letters 65, 182–202.

McKenzie, D., Jackson, J., Hancock, P.L., Williams, G.D., 1986. A block model of distributed deformation by faulting; Neotectonics. Journal of the Geological Society of London 143, 349–353.

Miller, D.D., 1998. Distributed shear, rotation, and partitioned strain along the San Andreas fault, central California. Geology 26, 867–870.

Molnar, P., 1992. Brace-Goetze strength profiles, the partitioning of strike-slip and thrust faulting at zones of oblique convergence, and the stress-heat flow paradox of the San Andreas fault. In: Evans, B., Wong, T. (Eds.), Fault Mechanics and Transport Properties of Rocks. Academy Press, San Diego, pp. 435–459.

Mount, V.S., Suppe, J., 1987. State of stress near the San Andreas fault: implications for wrench tectonics. Geology 15, 1143–1146.

Nilsen, T.H., Clarke, S.H., Jr., 1975. Sedimentation and Tectonics in the Early Tertiary Continental Borderland of Central California. U.S. Geological Survey Report P 0925.

Odonne, F., Vialon, P., 1983. Analogue models of folds above a wrench fault. Tectonophysics 99, 31–46.

Omarzai, S.K., 1996. Paleomagnetism Applied to the Monterey Formation of California. Ph.D. thesis, University of California Santa Cruz.

Onderdonk, N.W., 2005. Structures that accommodated differential vertical axis rotation of the Transverse Ranges, California. Tectonics 24, 15.

Page, B.M., 1981. The southern Coast Ranges. In: Ernst, W.G. (Ed.), The Geotectonic Development of California, Rubey Volume I. Prentice-Hall, Englewood Cliffs, NJ, United States, pp. 329–417.

Page, B.M., Thompson, G.A., Coleman, R.C., 1998. Late Cenozoic tectonics of the central and southern Coast Ranges of California. Geological Society of America Bulletin 110, 846–876.

Pisciotto, K.A., 1978. Basinal Sedimentary Facies and Diagenetic Aspects of the Monterey Shale, California. Ph.D. thesis, University of California Santa Cruz.

Pisciotto, K.A., Garrison, R.E., 1981. Lithofacies and depositional environments of the Monterey Formation, California. In: Garrison, R.E., Douglas, R.G. (Eds.), The Monterey Formation and related siliceous rocks of California. Society of Economic Paleontology and Mineralogy Pacific Section, Los Angeles, pp. 97–122.

Pollitz, F.F., 1986. Pliocene change in Pacific-Plate motion. Nature 320, 738–741.

Ramsay, D.M., 1979. Analysis of rotation of folds during progressive deformation. Geological Society of America Bulletin 90, I 732–I 738.

Richard, P., Mocquet, B., Cobbold, P.R., 1991. Experiments on simultaneous faulting and folding above a basement wrench fault. Tectonophysics 188, 133–141.

Sanderson, D.J., 1973. The development of fold hinges oblique to the regional trend. Tectonophysics 16, 55–70.

Sanderson, D.J., Marchini, W.R.D., 1984. Transpression. Journal of Structural Geology 6, 449–458.

Scholz, C.H., Cowie, P.A., 1990. Determination of the total strain from faulting using slip measurements. Nature 346, 837–839.

Snyder, W.S., 1987. Structure of the Monterey Formation; stratigraphic, diagenetic, and tectonic influences on style and timing: Cenozoic basin development of coastal California. In: Ingersoll, R., Ernst, W.G. (Eds.), Rubey Colloquium on Cenozoic Basin Development of Coastal California. Prentice-Hall, Englewood Cliffs, NJ, pp. 321–347.

Stamatakos, J.A., Hirt, A.M., Lowrie, W., 1996. The age and timing of folding in the central Appalachians from paleomagnetic results. Geological Society of America Bulletin 108, 815–829.

Taliaferro, N.L., 1943a. Bradley-San Miguel District. California Department of Natural Resources Division of Mines Bulletin 118, 456–462.

Taliaferro, N.L., 1943b. Geologic history and structure of the central Coast Ranges of California. California Department of Natural Resources Division of Mines Bulletin 118, 119–163.

Tavarnelli, E., Holdsworth, R.E., 1999. How long do structures take to form in transpression zones? A cautionary tale from California. Geology 27, 1063–1066.

Tauxe, L., Watson, G.S., 1994. The fold test: an eigen analysis approach. Earth and Planetary Science Letters 122, 331–341.

Terres, R.R., Luyendyk, B.P., 1985. Neogene tectonic rotation of the San Gabriel Region, California, suggested by Paleomagnetic vectors. Journal of Geophysical Research 90, 12,467–12,484.

Teyssier, C., Tikoff, B., 1998. Strike-slip partitioned transpression of the San Andreas fault system: a lithospheric-scale approach. In: Holdsworth, R.E., Strachan, R.A., Dewey, J.F. (Eds.), Continental transpressional and transtensional tectonics. Geological Society, London, Special Publications, vol. 135, pp. 143–158.

Teyssier, C., Tikoff, B., Markley, M., 1995. Oblique plate motion and continental tectonics. Geology 23, 447–450.

Tikoff, B., Fossen, H., 1993. Simultaneous pure and simple shear; the unifying deformation matrix. Tectonophysics 217, 267–283.

Tikoff, B., Peterson, K., 1998. Physical experiments of transpressional folding. Journal of Structural Geology 20, 661–672.

Tikoff, B., Teyssier, C., 1994. Strain modeling of displacement-field partitioning in transpressional orogens. Journal of Structural Geology 16, 1575–1588.

Treagus, J.E., Treagus, S.H., 1981. Folds and the strain ellipsoid: a general model. Journal of Structural Geology 3, 1–17.

Walsh, J., Watterson, J., Yielding, G., 1991. The importance of small-scale faulting in regional extension. Nature 351, 391–393.

Wilcox, R.E., Harding, T.P., Seely, D.R., 1973. Basic wrench tectonics. The American Association of Petroleum Geologists Bulletin 57, 74–96.

Zoback, M.D., Moos, D., Mastin, L., Anderson, R.N., 1985. Well bore breakouts and in situ stress. Journal of Geophysical Research 90, 5523–5530.

Zoback, M.D., Zoback, M.L., Mount, V.S., Suppe, J., Eaton, J.P., Healy, J.H., Oppenheimer, D.H., Reasenberg, P.A., Jones, L.M., Raleigh, C.B., Wong, I.G., Scotti, O., Wentworth, C.M., 1987. New evidence on the state of stress of the San Andreas fault system. Science 238, 1105–1111.